Structurally distinct manganese-sensing riboswitch aptamers regulate diverse expression platform architectures

Authors:

Christine N. Stephen[1], Danea E. Palmer[1], and Tatiana V. Mishanina[1*]

[1]Department of Chemistry and Biochemistry, University of California San Diego, 9500 Gilman Dr, La Jolla, CA 92093

***Corresponding author information:**

Phone: (858) 246-5883

Email: tmishanina@ucsd.edu

Abstract

Manganese (Mn)-sensing riboswitches protect bacteria from Mn toxicity by upregulating expression of Mn exporters. The Mn aptamers share key features but diverge in other important elements, including within the metal-binding core. Although X-ray crystal structures of isolated aptamers exist, these structural snapshots lack crucial details about how the aptamer communicates the presence or absence of ligand to the expression platform. In this work, we investigated the Mn-sensing translational riboswitches in *E. coli* (*mntP* and *alx*), which differ in aptamer secondary structure, nucleotide sequence, and pH-dependence of Mn response. We performed co-transcriptional RNA chemical probing, allowing us to visualize RNA folding intermediates that form and resolve *en route* to the final folded riboswitch. For the first time, we report that sampling of metal ions by the RNA begins before the aptamer synthesis and folding are complete. At a single-nucleotide resolution, we pinpoint the transcription window where “riboswitching” occurs in response to Mn binding and uncover key differences in how the *alx* and *mntP* riboswitches fold. Finally, we describe riboswitch-specific effects of pH, providing insights into how two members of the same riboswitch family differentially sense two distinct environmental cues: concentration of Mn and pH.

Introduction

Transition metal ions play key cellular roles (e.g., serving as enzyme cofactors) but become harmful in excess due to misincorporation into biomolecules and metal-catalyzed formation of reactive oxygen species[1,2]. To match the need for metal ion transporters, cells use the metal's intracellular concentration to regulate expression of the metal's transporters at the transcription and/or translation level[3]. Examples of this regulation include metal-binding transcription regulators[4,5] or direct interaction of the metal with a riboswitch encoded in the mRNA[6–8]. Riboswitches are 5'-untranslated regions of mRNA that promote or inhibit expression of the downstream gene by changing their folding upon binding a ligand[9]. A riboswitch is comprised of a ligand-binding aptamer overlapping with an expression platform, whose folding determines the transcriptional and/or translational fate of the mRNA[9]. Many classes of metal-sensing riboswitches have been identified, such as magnesium[7], nickel[8], cobalt[8], and manganese (Mn)[6,10].

The *yybP-ykoY* Mn-sensing riboswitch family is the largest metal-sensing family, with >1,000 unique representatives in different bacterial phyla[11]. Crystal structures, single-molecule FRET (smFRET), and molecular dynamics (MD) simulations of isolated Mn-sensing aptamers provided valuable insights into the overall RNA fold, metal binding site, and RNA dynamics in the presence or absence of Mn[12,13]. However, these studies lack the expression platform of the riboswitch – the "business end" that determines the gene expression outcome. Consequently, it remains unknown how Mn binding to the aptamer actuates the differential folding of the downstream RNA to affect its transcription or

70 translation. Further, studies to date were performed on pre-synthesized RNA, missing the
71 aspect of active transcription that is critical to riboswitch folding[14–17].

72 We addressed these gaps by investigating the two Mn-sensing translational
73 riboswitches in *E. coli* which regulate translation of the *alx* and *mntP* genes, with the *alx*
74 riboswitch upregulating gene expression in response to alkaline pH and increased Mn
75 concentration ([Mn])[18,19] (Fig. 1A). Binding of Mn to either the *mntP* or *alx* aptamers
76 promotes a translationally active conformation in the expression platform, increasing
77 expression of the Alx and MntP Mn exporters[10,19,20] (Fig. 1A-B). Multiple structures of Mn-
78 sensing riboswitch aptamers established their core structural features, consisting of two
79 coaxially stacked "legs" connected by a four-way junction (4WJ)[6,12,21] (Fig. 1C). The right
80 leg (L1, P1.1, P1.2, and P2; Fig. 1C) extrudes a conserved adenosine in L1 to form a
81 cross-helix A-minor interaction with P3.1 in the left leg (L3, P3.1, P3.2, and P4; Fig. 1C).
82 The L3 loop in the left leg stacks below the conserved adenosine in the A-minor
83 interaction, forming a phosphate-rich metal-binding hot spot (Fig. 1C). X-ray crystal
84 structures show two metal-binding sites in the aptamer, with one occupied by Mg^{2+} (M_A)
85 and the other by Mn^{2+} (M_B)[6,12,21] (Fig. 1C). The P1.1 "switch helix" is a key element of the
86 *yybP-ykoY* aptamer as its 3'-half alternatively pairs within the aptamer or the expression
87 platform depending on whether Mn is bound, with consequences to folding of the rest of
88 the expression platform.[12] (see Fig. 1B for *alx* and *mntP* alternative P1.1 pairing).

89 Despite sharing conserved features for Mn-sensing, the *alx* and *mntP* riboswitches
90 differ in their global architectures (Fig. 2A). The *alx*-like riboswitches are exclusively
91 present in the *Enterobacteriales* order, members of which are often found in environments

92 that can alkalinize, such as water, soil, and in association with other organisms[22,23]. Upon
93 alkaline pH challenge, the *E. coli* cytosol alkalinizes and then recovers to pH 7.8[24]; in turn,
94 cytosol alkalinization increases cytoplasmic [Mn][19], potentially explaining *alx* translational
95 activation at alkaline pH. Initial studies of the *alx* and *mntP* riboswitches put forward
96 alternative secondary structure models based on chemical probing with pre-synthesized
97 RNA[10,18], prompting us to ask (i) how these alternative structures fold and respond to Mn
98 during transcription and (ii) why alkaline pH uniquely affects *alx* structure. To answer
99 these fundamental questions, we applied modern RNA chemical probing methods to *alx*
100 and *mntP*, where ribonucleotides are modified by either a selective 2'-hydroxyl (SHAPE)
101 reagent or dimethyl sulfate (DMS) and detected by high-throughput mutational profiling
102 (MaP)[25].

103 In this work, we performed DMS-MaP in a co-transcriptional format using established
104 methods[26,27], getting to the heart of how Mn binding to the aptamer is "communicated" to
105 the expression platform. Unexpectedly, we uncovered evidence that both *alx* and *mntP*
106 aptamer folding intermediates begin sampling for divalents before the full aptamer domain
107 has emerged from RNAP, challenging the notion that a fully folded aptamer is required
108 for ligand sensing. Further, a critical RNA loop that participates in Mn sensing diverges in
109 sequence between *alx* and *mntP* and may hold the key to how pH differentially affects
110 riboregulation by these riboswitches. Using gene reporter assays, we show that alkaline
111 pH alone cannot rearrange the *alx* riboswitch into a translationally active conformation;
112 instead, the *alx* riboswitch senses the increased [Mn] brought about by alkaline pH. Lastly,
113 our co-transcriptional chemical probing data uncovered distinct structural features in the

114 *alx* and *mntP* expression platforms, which are potentially coupled to the cellular need for
115 the Alx and MntP exporter proteins under increased cytosolic [Mn].
116
117 **Results**
118 **The Mn-sensing aptamers of the *alx* and *mntP* riboswitches differ structurally**
119 In Fig. 2A, we present secondary structure models of the *alx* and *mntP* riboswitch aptamer
120 domains based on prior experimental data for the full-length riboswitches[10,18], which we
121 updated to reflect the overall aptamer architecture and conserved base-pairs identified by
122 X-ray crystal structures[6,12,21]. The model of the *mntP* aptamer in Fig. 2A is supported by
123 an X-ray crystal structure of the aptamer in the apo state (PDB ID: 4Y1M)[6]. Since no
124 detailed structural information exists for the *alx* aptamer, we mapped its secondary
125 structure with DMS/SHAPE-MaP using the traditional approach of *in vitro* synthesis by T7
126 RNA polymerase (RNAP) followed by denaturation and refolding.
127
128 *pH and Mn effect on the alx aptamer structure.* The aptamer RNA was refolded at either
129 neutral (7.2) or alkaline pH (8.5) data and *in vitro* transcription experiments[18,28] and the
130 alkaline pH value aligns with published gene reporter and *in vitro* transcription
131 experiments[19,28]. The aptamer RNAs were probed with either 1-methyl-7-nitroisatoic
132 anhydride (1M7) or DMS. The resulting secondary structure models of the *alx* aptamer
133 agree with the published 2D predictions[18] and 3D structure of an *L. lactis* chimera with
134 the *alx* L3 sequence[21] (Fig. 2B and SI Fig. 1A-C). Comparison of the nucleotide (nt)
135 reactivities as a function of refolding pH revealed clear flexibility differences in L3 and L1,

136 with multiple nt (e.g., A37 and A11) showing decreased reactivity towards 1M7 or DMS
137 at alkaline pH (Fig. 2C).

138 We next refolded the *alx* aptamer RNA at either neutral (7.2) or alkaline pH (8.5) in the
139 presence of 1 mM $MnCl_2$ and probed with either DMS or 1M7. While the total physiological
140 [Mn] (free and bound) in *E. coli* is estimated to be 15-21 μM[29–31], we chose a saturating
141 concentration of ligand to maximize the ligand-induced shift in the RNA conformational
142 ensemble, consistent with prior chemical probing experiments on other riboswitches[27,32].
143 $MgCl_2$ was present at 5 mM in the RNA refolding buffer, thus Mg remained in excess of
144 Mn, as is the case *in vivo*[33]. We observed L3 generally becomes less reactive towards
145 1M7 in the presence of Mn, consistent with reduced flexibility upon Mn binding (SI Fig.
146 1D). Interestingly, in the presence of Mn, pH-dependent reactivity changes for multiple
147 L1/L3 nt are abolished (e.g., A37 and A11, Fig. 2C), supporting that these nt are buried
148 in the metal-sensing core with Mn and consistent with published Mn-bound aptamer
149 structures[6,12,21] (see Supplementary Note 1 and SI Fig. 1E for additional analysis).

150

151 *Structural comparison of the alx and mntP aptamers.* Despite belonging to the same
152 family, the *alx* and *mntP* riboswitch aptamers harbor intriguing structural differences. First,
153 the *alx* aptamer contains an intrinsic termination site in the P4 helix[28], which occurs before
154 the metal-sensing pocket forms (Fig. 2A). The *alx* aptamer lacks the P2 helix, resulting in
155 a three-way junction (3WJ) rather than a 4WJ in the *mntP* aptamer and all other aptamers
156 studied by X-ray crystallography. Lastly, the L3 sequences in *alx* and *mntP* metal-sensing
157 cores differ (Fig. 1C), raising the possibility that L3 tunes Mn affinity of the aptamer.

158 **Transcription by native RNA polymerase is required for *alx* and *mntP* riboswitch-**
159 **mediated translational regulation *in vivo***

160 We next wondered whether *alx* and *mntP* riboregulation is kinetically controlled. To test
161 this, we constructed *alx* and *mntP* translational *lacZ* reporters cloned with either the T7
162 promoter or native *alx/mntP* promoter into single copy plasmids (Fig. 2D). The effect of
163 extracellular alkaline pH or elevated [Mn] on gene expression was measured by β-
164 galactosidase assays in either an *E. coli* strain (MC4100) lacking *alx* (Δ*alx*), to preclude
165 negative autoregulation[19], or the Δ*alx* strain with T7 RNAP expressed from the *lac*
166 promoter (chromosomally encoded, Δ*alx*T7). The plasmids containing the native
167 promoter translational reporters were transformed into the Δ*alx* strain and the plasmids
168 containing the T7 promoter translational reporters were transformed into the Δ*alx*T7
169 strain. The strains were cultivated in i) neutral pH (LBK pH 6.8) or alkaline pH (LBK pH
170 8.4) media, and ii) neutral pH (LBK pH 6.8) media with supplemented $MnCl_2$.

171 We observed the expected changes in *alx* and *mntP* translation in response to pH
172 and supplemented $MnCl_2$ when reporter fusions were transcribed from their native
173 promoters[19] (Fig. 2E-F). While only *alx* translation was induced by alkaline pH, translation
174 of both genes increased with supplemented $MnCl_2$ (Fig. 2E-F). Strikingly, transcription by
175 T7 RNAP abolished the response to alkaline pH and/or Mn (Fig. 2E-F), demonstrating
176 that faster transcription of the *alx* and *mntP* riboswitches (~220 nt/s; T7 RNAP[34] vs. ~20-
177 90 nt/s; *E. coli* RNAP[35]) prevents riboswitching in response to alkalinization and/or
178 elevated [Mn] in the cytosol. In sum, these data establish that transcription by *E. coli*

179 RNAP is required for ligand-coupled structural rearrangements in the *alx* and *mntP*
180 expression platforms.
181
182 **Analysis of the *mntP* aptamer folding during transcription using co-transcriptional**
183 **chemical probing**
184 To investigate both pH and Mn-mediated structural changes in the *alx* and *mntP*
185 riboswitch folding intermediates, we performed co-transcriptional chemical probing
186 (variable length Transcription Elongation Complex RNA structure probing TECprobe-VL
187 method, see SI Fig. 2 for construct designs)[27]. Co-transcriptional chemical probing
188 experiments were performed at both neutral (7.2) and alkaline pH (8.5) ± 1 mM $MnCl_2$
189 (referred to as "+Mn" or "–Mn" condition, respectively) with 10 mM $MgCl_2$ present to
190 prevent compromised transcription fidelity from Mn-coordination by RNAP, as observed
191 for DNA polymerases[36] and reverse transcriptases[37]. Since published work established
192 that pH≥ 8 renders all 4 nucleobases accessible to DMS modification[38], we first present
193 data for *alx* and *mntP* DMS-probed folding intermediates at pH 8.5.
194
195 *The two legs of the Mn aptamer fold differently.* We initially mapped *mntP* aptamer folding
196 transitions and determined the specific transcript lengths where helices in the aptamer
197 become stably folded (Fig. 3A-B and SI Fig. 3). P3.1, P3.2, and P4 in the left leg of the
198 aptamer fold first, as detected with coordinated drops in reactivity of nucleotides that are
199 base-paired in these helices (Fig. 3C). In stark contrast, the right leg of the aptamer folds
200 into transient, low-melting temperature (T_m) stem-loops that form and resolve until the

201 synthesis of the aptamer is completed (~nt 124, assuming a 14-nt RNAP footprint, Fig.
202 3B). While the 5' RNA stretch for these aptamer elements (L1, P1.1, and P1.2) is
203 transcribed early on, their 3' pairing partner does not emerge from RNAP until late in
204 transcription. Thus, the weak stem-loop intermediates may prevent RNA from being
205 trapped in stable but not biologically relevant folds, consistent with other riboswitches[16,27].
206 P2 in the right leg folds towards the end of aptamer transcription, even though the
207 sequence encoding P2 emerges at transcript length ~50 nt, indicating that folding of the
208 entire right leg occurs at the end of aptamer synthesis (Fig. 3C).
209
210 *RNA folding intermediates sample for Mn.* Surprisingly, we observed Mn-dependent
211 differences in reactivity of several nucleotides *before* complete *mntP* aptamer has been
212 synthesized (Fig. 3D). For example, A48, the first nucleotide in the L3 loop, demonstrates
213 markedly high reactivity ±Mn, with its reactivity trending higher +Mn starting at transcript
214 length ~115 nt – before the aptamer synthesis finished ~124 nt (Fig. 3D). We hypothesize
215 that this is indicative of an RNA folding intermediate sampling divalent metal ions in
216 solution in search for Mn, with its L3 and partially formed L1/P1.1. Such partial binding of
217 Mn was observed in a crystal structure and molecular dynamics (MD) simulations of the
218 full-length *X. oryzae* aptamer, referred to as "conformer 2", which lacks the ordered
219 stacking pattern in L3 and contains a partially dehydrated Mn in the M_B site[12] (Fig. 3D).
220 The partially dehydrated Mn lacks half of the contacts seen in "conformer 1" (coordinated
221 to fully dehydrated Mn); however, the inner sphere contact between the phosphate of the
222 first nucleotide in L3 and the metal is observed (A48 in *E. coli mntP* aptamer vs. A46 in

223 *X. oryzae* aptamer)[12]. Therefore, A48 can contact a partially dehydrated Mn before the
224 full aptamer is synthesized, explaining its Mn-dependent reactivity differences in *mntP*
225 aptamer folding intermediates. U54 in L3 and A103 in L1 also show Mn-dependent
226 reactivity differences in aptamer intermediates, with their reactivities trending higher –Mn
227 (Fig. 3D). These reactivity differences can be explained by greater conformational
228 flexibility in the metal-binding site (see Fig. 3D for U54 and A103 positioning in *X. oryzae*
229 conformers 1 and 2). Additionally, we observed multiple RNAP pauses preceding *mntP*
230 aptamer completion that are enhanced by the presence of Mn and may mediate partial
231 Mn binding/ sampling of divalents in the environment by the RNA (see Supplementary
232 Note 2 and SI Figs. 4-5 for further analysis).

233 To identify the intermediates whose folding is truly controlled by transcription kinetics
234 vs. thermodynamic stability of the folds, we applied a modified TECprobe-VL workflow
235 wherein intermediate RNA transcripts are extracted from the stalled transcription
236 elongation complexes and equilibrium refolded before DMS probing. These experiments
237 identified clear structural differences between co-transcriptionally folded and equilibrium
238 refolded *mntP* intermediates and provided additional evidence of divalent sampling by
239 aptamer folding intermediates (see Supplementary Note 3 and SI Fig. 6 for further
240 analysis).

241

242

243

244 **Analysis of the *alx* aptamer folding during transcription using co-transcriptional**
245 **chemical probing**

246 We next investigated the *alx* aptamer folding transitions at pH 8.5 (Fig. 4A-B and SI Fig.
247 7). Here, P3.1, P3.2, and P4 in the left leg fold first as the aptamer is extended from ~80
248 nt to ~125 nt (Fig. 4B-4C). Like in the *mntP* aptamer, the 5' end of the right leg folds into
249 transient, low-T_m stem-loops that resolve once the full-length aptamer RNA has emerged
250 from RNAP (Fig. 4B), highlighting a potentially conserved mechanism of the *yybP-ykoY*
251 aptamer folding.

252

253 *L3 flexibility differs between alx and mntP aptamers.* Like with *mntP*, we captured Mn-
254 dependent reactivity differences for L3 in *alx* aptamer folding intermediates (Fig. 4D). For
255 example, the reactivity of U35, the first nt in the *alx* L3, trends higher +Mn starting at
256 transcript lengths as short as ~50 nt (Fig. 4D). This trend mimics that seen with the first
257 nt in *mntP* L3, A48, with a few key differences. First, the absolute reactivity values ±Mn
258 are greater for A48 in *mntP* L3 (Fig. 3D). Second, the increased reactivity +Mn occurs
259 much earlier for *alx* aptamer intermediate transcript lengths (~50 nt for *alx* vs. ~115 nt for
260 *mntP*). The absolutely conserved adenosine in *alx* L3 that directly coordinates Mn (A37)
261 is more reactive –Mn for aptamer folding intermediates starting at transcript length ~70 nt
262 (Fig. 4D). The higher A37 reactivity –Mn is consistent with greater L3 flexibility in this
263 condition and further supports that the L3 loop can begin sampling for divalents before
264 the aptamer domain is fully folded. Curiously, the absolutely conserved adenosine in
265 *mntP* L3 (A50) does not demonstrate this Mn-dependent reactivity difference (Fig. 3C),

266 pointing to a difference in L3 dynamics between *alx* and *mntP* aptamer folding
267 intermediates. Similar to *mntP*, we observed clear structural differences between co-
268 transcriptionally folded and equilibrium refolded *alx* intermediates (see Supplementary
269 Note 4 and SI Fig. 8 for further analysis).
270

271 **Mn binding is a prerequisite for *alx* riboswitch pH response**

272 Early work characterized the *alx* riboswitch as a pH sensor[18]; however, recent studies
273 have called this into question[19]. Since the intracellular [Mn] increases in *E. coli* at alkaline
274 pH[19], we wondered whether the *alx* riboswitch is actually sensing the increase in [Mn] as
275 a consequence of cytosol alkalinization. To test this, we performed translational *lacZ*
276 reporter assays on the A37U *alx* mutant, where the absolutely conserved adenosine that
277 directly coordinates Mn in L3 is replaced with a uridine. This point mutation was previously
278 shown to ablate Mn-sensing in the *X. oryzae* aptamer[12] making it the best candidate
279 mutation to decouple the effect of Mn and alkaline pH on *alx* riboregulation *in vivo*.
280 Strikingly, the 68-fold increase in *alx* reporter translation observed upon a shift from pH
281 6.8 to 8.4 for the wild-type riboswitch was abolished by the A37U mutation (Fig. 5A).
282 These data provide the first evidence that the *alx* riboswitch is not a true pH sensor;
283 instead, the riboswitch senses increased cytosolic [Mn], which is an indirect effect of
284 cytosol alkalinization. Published *alx* translational reporter data showed an additive effect
285 of alkaline pH and Mn[19]. We thus hypothesize that alkaline pH enhances the affinity of
286 the *alx* aptamer for Mn, rather than alters the *alx* riboswitch folding, unifying observations
287 from early studies on this system[18,39] with a recently published genetic study[19]. A

288 combination of alkaline pH and high [Mn] produced higher *mntP* reporter translation
289 compared to the neutral pH condition with added Mn, suggesting that alkaline pH may
290 also enhance Mn affinity for the *mntP* aptamer, but to a lesser degree than for the *alx*
291 aptamer[19]. To explore this intriguing point further, we DMS-probed the *alx* and *mntP*
292 folding intermediates at pH 7.2 ±Mn with the TECprobe-VL method, as described in the
293 following section.
294
295 **pH effects on the *alx* and *mntP* aptamer folding: L3**
296 We largely observed the same co-transcriptional folding transitions for the two legs in the
297 *alx* and *mntP* aptamers at pH 7.2 as described for pH 8.5 (SI Fig. 9A-B). Although the *alx*
298 and *mntP* aptamers exhibit the same global folding transitions at pH 7.2, key pH-
299 dependent reactivity differences in their metal-sensing cores emerged. Here, we focused
300 on A and C nucleotide reactivities since G and U nucleotides are protonated at the
301 respective N1 and N3 positions at neutral pH and are thus unreactive towards DMS (pKa
302 ~ 9.2[40]). First, the absolutely conserved adenosine in the *alx* L3 (A37) exhibits a general
303 Mn-dependent reactivity decrease during aptamer folding at both pH (Fig. 5B). However,
304 the magnitude of this reactivity decrease is clearly pH-dependent, with A37 consistently
305 less reactive at pH 8.5 +Mn compared to other conditions tested (Fig. 5B), suggesting a
306 potentially more stable A37-Mn coordination at alkaline pH. In stark contrast, the
307 absolutely conserved adenosine in *mntP* L3 (A50) shows no drop in reactivity at pH 8.5
308 +Mn; instead, A50 lacks clear pH-dependent reactivity trends during aptamer folding (Fig.
309 5C). The first L3 nucleotide in the *mntP* aptamer (A48) is more reactive +Mn vs. –Mn

310 regardless of pH (Fig. 5C), supporting that A48 stacked with A11 in an Mn-bound, ordered
311 metal-sensing core increases its DMS reactivity. Interestingly, the absolute reactivity
312 values for A48 are markedly lower at pH 7.2 ±Mn (Fig. 5C), suggesting that A48 has an
313 upwardly shifted pK_a close to physiological pH (~pH 7.4-7.8 for *E. coli*[23]). We thus
314 hypothesize that deprotonation of A48 at alkaline pH promotes its stacking with A11 in
315 the cross-helix A-minor interaction, favoring docking of the helical legs in the aptamer
316 (see Supplementary Note 5 and SI Figs. 9C-D,10, and 11 for further analysis of pH-
317 dependent structural changes in *alx/mntP* L1 and L3 in co-transcriptionally folded vs.
318 equilibrium refolded aptamer intermediates).

319 We wondered whether L3 sequences in *Enterobacteriales yybP-ykoY* family members
320 show a unique trend that could explain the pH-dependent reactivity differences in the *alx*
321 and *mntP* aptamers. We aligned sequences of *yybP-ykoY* riboswitch family members
322 within the *Enterobacteriales* order, revealing two distinctive groups: an *alx*-like group
323 (consensus: UCAUUAC, Fig. 5D) and an *mntP*-like group (consensus: ACAUACU, Fig.
324 5D). We then compared the above sequences to the *yybP-ykoY* riboswitch family L3
325 consensus sequence generated from 1,063 aligned sequences (consensus: ACAUACU,
326 Fig. 5D). Generally, the first nucleotide in L3 is an A – an important position since this
327 nucleotide stacks with the conserved A11 in L1 that forms the cross-helix A-minor
328 interaction. Therefore, this position being strictly a U in *alx*-like members suggests a
329 functional role. Since the N3 of U has a close-to-physiological pKa of ~9.2[40], it is possible
330 that a shift from neutral to alkaline pH alters its stacking with the conserved A11 and
331 consequently Mn-coupled structural rearrangements in the expression platform.

332 **Analysis of *mntP* expression platform folding during transcription**

333 *Cross-helix A-minor disruption at the riboswitching point.* The expression platform for the
334 *mntP* riboswitch contains a single helix that begins folding at transcript length ~175 nt and
335 was detected by coordinated drops in reactivity for its constituent nucleotides (Fig. 6A
336 and Fig. S12A). In the absence of Mn, the aptamer remains stably folded for most of
337 expression platform synthesis until the transcript is ~205 nt long (Fig. 6B). At this critical
338 decision point – the riboswitching point – the L1 and P1.1 elements of the aptamer are
339 disrupted if no Mn is available, allowing for alternative pairing of P1.1 switch helix in the
340 expression platform (Fig. 6C). The disruption of P1.1 in the absence of Mn is consistent
341 with previously published single-molecule fluorescence experiments with an isolated
342 aptamer that show that this helix is less stable without Mn[12]. Analysis of single-nucleotide
343 trajectories revealed that A11 reactivity transiently spikes at ~205 nt, whether or not Mn
344 is included in the transcription reaction, but the amplitude of the spike is Mn-dependent
345 (Fig. 6D). The spike in A11 reactivity coincides with P1.1 strand invasion and its reduced
346 amplitude +Mn indicates A11 remains trapped in the long-range A-minor interaction in
347 Mn-bound aptamer. The L1/P1.1 reactivity difference heatmap ±Mn highlights A11 as the
348 nucleotide most sensitive to the presence of the ligand, serving as a marker for the
349 riboswitching point (Fig. 6D). We also assessed reactivity changes for A48 in L3 during
350 expression platform folding, since A48 stacks with A11 and helps anchor the cross-helix
351 A-minor interaction. A48 reactivity drops ±Mn starting at transcript length ~185 nt, with a
352 larger decrease –Mn (Fig. 6E). A48 reactivity is consistently lower –Mn for the remainder
353 of expression platform folding (Fig. 6E), likely due to broken A48-A11 stacking.

354 We observed similar reactivity trends in *mntP* expression platform folding at pH 7.2 as
355 pH 8.5 (e.g., A11 reactivity spike, SI Fig. 12B-C) and uncovered additional evidence of
356 P1.1/L1 disruption in the vicinity of the riboswitching point (see Supplementary Note 6
357 and SI Fig. 12D). Taken together, our observations highlight that a global structural
358 change occurs in the *mntP* expression platform at transcript lengths ~200-205 nt, which
359 is likely prompted by the start of strand invasion at P1.1 in the aptamer (see
360 Supplementary Note 6 and SI Fig. 12D for additional analysis of pH- and Mn-dependent
361 reactivity changes in *mntP* L1, L3, and P1.1 during expression platform folding).
362
363 *Co-transcriptional binding of Mn is required for riboswitching.* We next evaluated the
364 differences between co-transcriptionally folded and equilibrium refolded *mntP*
365 intermediate transcripts that contain both the aptamer domain and expression platform,
366 to assess whether co-transcriptional folding is required to observe Mn-coupled structural
367 rearrangements in the expression platform. While we observed similar P5 folding
368 transitions (SI Fig. 13A-B), the Mn-dependent spike in A11 reactivity is abolished when
369 the RNA is equilibrium refolded ±Mn at either pH 7.2 or 8.5 (SI Fig. 13C). These data
370 support that co-transcriptional Mn-binding is critical for stabilization of the A-minor motif
371 that docks the two legs of the aptamer together and for prevention of the P1.1/L1 invader
372 strand from disrupting the aptamer (see Supplementary Note 7 and SI Fig. 13D for
373 reactivity analysis of the A11 stacking partner, A48, in equilibrium refolded intermediates).
374 Further supporting the above observations, we found that T7-synthesized, equilibrium

375 refolded *mntP* riboswitch adopts a translationally inactive conformation ±Mn (DMS/1M7-
376 probed, described further in Supplementary Note 8 and SI Fig. 14).
377
378 **Analysis of *alx* expression platform folding during transcription**
379 *Distinct features of the alx expression platform folding.* The expression platform for the
380 *alx* riboswitch contains multiple helices that begin folding at transcript length ~155 nt, as
381 detected by coordinated drops in reactivity for the constituent nucleotides in each helix
382 (Fig. 7A and SI Fig. 15A). The *alx* expression platform contains two helices (termed here
383 P5 and P6) in its translationally inactive conformation that are predicted to fold –Mn,
384 resulting in the ribosome binding sequence (RBS) base-paring with a disrupted P1.1/L1
385 (Fig. 7B-D). On the other hand, when P1.1/L1 remain base-paired in the Mn-bound *alx*
386 aptamer, an alternative helix in the expression platform (termed here P5/P6) is predicted
387 to fold, and the downstream RBS-containing strand is single-stranded (Fig. 7E-G).
388 Unlike the *mntP* riboswitch, the *alx* P1.1/L1 rising stem is highly dynamic during the
389 entirety of *alx* expression platform folding both ±Mn, which was detected as consistent
390 reactivity towards DMS for multiple nt (Fig. 7A). The strand predicted to invade P1.1/L1
391 in the *alx* aptamer emerges at transcript length 155 nt, resulting in formation of the P5
392 helix (Fig. 7A). Once the expression platform is extended to transcript length 190 nt, the
393 P6 intrinsic terminator helix folds (Fig. 7A). Interestingly, the DMS reactivities for
394 nucleotides in the *alx* expression platform were largely similar ±Mn, resulting in similar
395 secondary structure predictions for expression platform folding intermediates (SI Fig.
396 15B-D).

397 Despite the global structural similarities in the *alx* expression platform secondary
398 structural models ±Mn, we detected multiple Mn-dependent reactivity differences for
399 specific nucleotides that indicate a modest ligand-dependent shift in the conformational
400 ensemble. P5 stem-loop nucleotides are more reactive –Mn (Fig. 7C), consistent with a
401 population bias towards the inactive conformer. A137 (bulged in active conformer vs.
402 base-paired in inactive conformer) demonstrates markedly high reactivity in general and
403 exhibits higher reactivity +Mn (Fig. 7F), indicating a shift in the conformational ensemble
404 towards the *alx* active conformer.
405
406 *pH effects during folding of the alx expression platform.* We observed similar DMS
407 reactivity patterns in the *alx* expression platform at neutral vs. alkaline pH, such as folding
408 of P5 and P6 (SI Fig. 16A-B), indicating that a shift to alkaline pH impacts metal-sensing
409 rather than directly affecting folding of the expression platform and thus riboswitching.
410 However, we observed interesting pH-dependent reactivity trends for A137, which was
411 more reactive +Mn at both pH and most reactive overall at pH 8.5 +Mn (SI Fig. 16B),
412 supporting that the active conformer is sampled more frequently under this condition.
413 We next assessed pH- and Mn-dependent reactivity trends in the *alx* aptamer during
414 expression platform folding (Fig. 8A-C). Contrasting *mntP*, A11 remains accessible for
415 DMS methylation across all conditions tested with no significant pH and Mn-dependent
416 differences (Fig 8B and SI Fig. 16C). Since A11 is conserved in *alx* and *mntP* L1, it is
417 curious that A11 exhibits distinctive reactivity trends between the two riboswitches. Unlike
418 in *mntP*, the absolutely conserved A37 in *alx* aptamer remains least reactive at pH 8.5

419 +Mn for the duration of expression platform folding (supportive of more stable Mn binding
420 at alkaline pH), with multiple transient spikes in reactivity indicating a change in L3
421 dynamics at pH 8.5 +Mn during expression platform folding (Fig. 8C and SI Fig. 16C).
422 Additionally, we observed interesting pH- and Mn-dependent reactivity trends for *alx*
423 expression platform nt in equilibrium refolded intermediates (see Supplementary Note 9
424 and SI Fig. 17).
425
426 **The *mntP* and *alx* RBS regions are dynamic in co-transcriptionally displayed RNA**
427 The RNA surrounding the *mntP* RBS did not demonstrate a clear Mn-dependent reactivity
428 trend, with DMS-constrained structure models predicting low-T_m hairpins interspersed
429 with single-stranded regions (Fig. 18A). We thus conclude that the RNA around the RBS
430 is dynamic, and any Mn-dependent structural differences are likely averaged out. Prior
431 smFRET study observed such RBS dynamics for the $preQ_1$ translational riboswitch with
432 ligand-dependent accessibility bursts in the RBS region[41]. Therefore, characterization of
433 the *mntP* RBS dynamics requires complementary, e.g., single-molecule methods.
434 Likewise, heatmap visualization of the *mntP* RBS nucleotides at pH 7.2 or 8.5 ±Mn or in
435 equilibrium refolded intermediates at both pH showed no clear reactivity difference that
436 would indicate increased RBS accessibility +Mn (SI Fig. 18B-C).
437 For *alx*, the presence of the P6 intrinsic terminator stem resulted in a stark decrease
438 in representation for longer transcripts containing the RBS (SI Fig. 19A), precluding
439 accurate modeling of the RNA structure in this region. To boost representation of full-
440 length *alx*, we performed a modified co-transcriptional chemical probing experiment with
441 a terminally biotinylated DNA template and the fast-acting SHAPE reagent benzoyl

442 cyanide (BzCN, reaction time ~1s) to better capture the short-lived co-transcriptional, Mn-
443 dependent structural changes in the RBS. Consistent with *mntP*, the single-length BzCN
444 probing experiment revealed no clear Mn-dependent differences in the reactivities of RBS
445 nucleotides (Fig. 19B), supporting that the *alx* RBS is dynamic. These dynamics may
446 serve a functional role; for instance, the RBS may be rapidly docking/undocking with
447 another tertiary structural element in *alx*, with the docking rate fine-tuning RBS
448 accessibility. Underscoring the importance of co-transcriptional chemical probing, we
449 found that T7-synthesized, equilibrium refolded *alx* riboswitch adopts a translationally
450 inactive conformation ±Mn (DMS/1M7-probed, described further in Supplementary Note
451 10 and SI Fig. 20). Taken together, while *alx* and *mntP* differ structurally, they may share
452 common dynamic features that gate RBS accessibility.
453

454 **Discussion**

455 In this work, we performed a suite of chemical probing experiments on the Mn-sensing
456 translational riboswitches in *E. coli* that precede the *mntP* and *alx* genes encoding Mn
457 exporters. While static structural snapshots are available for Mn-sensing aptamers, these
458 structures do not answer the question of how binding of Mn to the aptamer is
459 "communicated" to the expression platform – the question at the heart of riboswitch
460 function. Because the *mntP* and *alx* aptamers display unique architectures, they are an
461 interesting test case of how structurally distinct aptamers in the same riboswitch family
462 "talk" to the expression platform. We demonstrated that co-transcriptional folding with the
463 native *E. coli* RNAP is essential for Mn-coupled structural rearrangements in the *mntP*

464 and *alx* riboswitches *in vivo*, which prompted us to perform co-transcriptional chemical
465 probing experiments.

466 The co-transcriptional chemical probing revealed that 5'-proximal halves in both *alx*
467 and *mntP* aptamers traverse low-T_m RNA hairpin intermediates during folding,
468 presumably as a safeguard against premature folding of RNA into stable but non-
469 functional folds. Surprisingly, we found that both riboswitches show Mn-dependent
470 reactivity changes *before* the full aptamer domain has folded. The Mn-dependent
471 structural changes in aptamer folding intermediates map to nucleotides in the *alx* and
472 *mntP* metal-sensing cores, indicating that a partially formed metal-sensing core can
473 interrogate the environment for Mn. Curiously, these Mn-dependent differences emerge
474 at much earlier transcript lengths for *alx* aptamer folding, which may permit a rapid
475 response to the subtle increase in [Mn] prompted by cytosol alkalinization[19].

476 Notably, other riboswitches that have been investigated with co-transcriptional
477 SHAPE-seq or SHAPE-MaP (ZTP, ppGpp, and fluoride) did not show ligand-dependent
478 structural changes for folding intermediates[27]. Ligands such as ZTP and ppGpp are larger
479 than an Mn ion and require a network of interactions to bind their cognate aptamers[42,43].
480 The resulting structural complexity of these aptamer-ligand interactions likely prevents
481 their stable interaction with an aptamer folding intermediate. In the case of fluoride
482 riboswitch, binding of fluoride anion to the aptamer is mediated by a network of Mg^{2+} ions
483 to overcome steric repulsion by the phosphate backbone[44], making fluoride less likely to
484 bind an aptamer folding intermediate. Additionally, it will be interesting to see whether

485 other divalent-sensing riboswitches (e.g., Mg^{2+}- and Ni^{2+}/Co^{2+}-sensing riboswitches) can
486 begin sampling for ligand before the complete aptamer has folded.

487 To get at the molecular basis of the divergent pH response of the *alx* and *mntP*
488 riboswitches, we performed co-transcriptional DMS probing of RNA at both neutral and
489 alkaline pH ±Mn. We found that pH uniquely affects the structure of the *alx* and *mntP*
490 metal-sensing cores, providing the first clues to how pH differentially affects Mn sensing.
491 The *alx* and *mntP* aptamers differ in their global architecture, forming a 3WJ and a 4WJ,
492 respectively. Future study should investigate how nucleobase protonation states in the
493 *alx* and *mntP* metal-sensing cores are coupled to junction dynamics, which controls the
494 docking of the aptamer's helical legs. Prior smFRET study on the *X. oryzae* aptamer, a
495 4WJ aptamer like *mntP*, illustrated how Mn binding promotes docking of the two helical
496 legs that in turn stabilizes the P1.1 switch helix[12]. The dynamics of *alx*-like aptamers has
497 not yet been studied but may play a role in the differential pH effect on *alx* vs. *mntP* Mn
498 sensing and consequent riboswitching.

499 The stark differences in the flexibility, architecture, and pH/Mn response of the
500 *mntP* vs *alx* riboswitches may be coupled to the cellular function of their respective Mn
501 exporters. We showed that alkaline pH alone does not rearrange the *alx* riboswitch into a
502 translationally active conformer; rather, the *alx* riboswitch senses the increased cytosolic
503 [Mn] brought about by cytosol alkalinization. We hypothesize that alkaline pH lowers the
504 K_D of the *alx* aptamer for Mn, explaining why an alkaline pH shift and consequent increase
505 of [Mn] from 28 to 42 μM (free and bound) activates expression of *alx* but not *mntP*[19] (Fig.
506 9). The physiological functions of such pH-enhanced expression of Mn exporters could

507 be multi-fold. For example, Mn(II) is oxidized at alkaline pH[45,46], deeming it unusable by
508 Mn-dependent enzymes. Further, oxidized Mn(IV) is an extremely reactive agent able to
509 oxidize carbon-carbon double bonds in nucleobases, the capability exploited in
510 permanganate footprinting of protein-nucleic acid complexes[47,48]. Removal of Mn by
511 exporters to minimize the pool of oxidized Mn could thus be a protective measure for the
512 cell experiencing alkaline stress.
513
514 *Limitations of this study*. There are multiple limitations to the experimental approaches
515 used here. First, co-transcriptional chemical probing experiments are an endpoint
516 measurement and do not capture the true structural intermediates traversed by an RNA
517 during transcription. Further, the DMS probing reaction is 5 min., meaning that the co-
518 transcriptionally displayed RNA can equilibrate to some degree. As a control, we
519 performed DMS probing experiments on equilibrium refolded intermediates, which
520 showed structural differences. However, we cannot rule out the possibility that the RNA
521 folds observed with co-transcriptional DMS probing are not always representative of a
522 true folding intermediate. Lastly, since the DMS probing reactions were performed *in vitro*,
523 the absence of ribosomal proteins may have altered the observed structural ensemble,
524 which should be addressed in future work.
525

Methods

The source and catalog number (if applicable) for all key reagents are provided as a Supplementary Table 1.

All oligonucleotides were purchased from either Integrated DNA Technologies or Eton Bioscience. A summary of all oligonucleotides used in this work including sequences, modifications, and purifications is presented in Supplementary Table 2.

Procedures for protein preparations, construction of plasmids and bacterial strains, and preparation of DNA templates are provided in the Supplemental Methods.

Single-round *in vitro* transcription for TECprobe-VL experiments

To prepare the holoRNAP, *E. coli* RNAP (6 μM) and σ^{70} (12 μM) were combined in 1x TECprobe transcription buffer (100 mM Tris-Cl, pH 7.2 or 8.5, 50 mM KCl, and 1 mM DTT) and incubated for 30 min at 37 °C. The single-round *in vitro* transcription reactions for TECprobe-VL experiments were assembled by first combining 1x transcription buffer, 40 nM DNA template (*alx* riboswitch, Template 3, Supplementary Table 3) or 50 nM DNA template (*mntP* riboswitch, Template 6, Supplementary Table 3) with randomly distributed internal biotin-11 dNMPs (AAT BioQuest/Biotium), 0.5 μM holoRNAP, and 500 μM ATP, UTP, CTP, and GTP. The transcription buffer omitted magnesium, which was a part of the start solution added later to initiate transcription elongation. Tris-Cl was added at a final concentration of 100 mM to minimize pH changes during the chemical probing reaction, as described previously[27]. The reaction was incubated for 10 min at 37 °C to form open promoter complexes. Next, SAvPhire Monomeric Streptavidin (Sigma-Aldrich) was added to the reaction at a final concentration of 5 μM, followed by incubation for 10 min at 37 °C to allow streptavidin binding to biotinylation sites on the DNA template. Transcription was initiated by adding 10X start solution (100 mM $MgCl_2$, 100 μg/ml rifampicin) to the reaction to a final concentration of 10 mM $MgCl_2$ and 10 μg/ml rifampicin to inhibit reinitiation. After addition of start solution, the final reaction volume was 60 μl. To test the effect of the Mn ligand on riboswitch structural rearrangements, $MnCl_2$ was added to a final concentration of 1 mM in the transcription reactions and was introduced alongside the start solution. The transcription reaction was incubated for 30 s at 37 °C before proceeding to the chemical probing, which is described in the next section.

Single-round *in vitro* transcription for the single-length TECprobe-SL experiments followed the same protocol as outlined above for variable length TECprobe-VL experiments. The DNA templates used for TECprobe-SL experiments contained a terminal biotin modification that was introduced by a 5' biotinylated reverse primer in the PCR (*alx* riboswitch, Template 7, Supplementary table 3).

570 **RNA chemical probing during TECprobe-VL experiments**
571
572 Benzoyl cyanide (BzCN, Sigma-Aldrich) probing was performed by splitting the 60-μl
573 transcription reaction into 25 μl aliquots and mixing with either 2.78 μl of 400 mM BzCN
574 dissolved in anhydrous DMSO (Invitrogen) to a final concentration of 17.7 mM [(+)
575 sample] or with anhydrous DMSO [(-) sample]. Since the BzCN probing reaction is
576 complete within ~1 s, no additional incubation was required before quenching the
577 reactions with 250 μl of TRIzol reagent (Invitrogen).
578
579 DMS probing was performed by splitting the 60-μl transcription reaction into 25 μl aliquots
580 and mixing with either 2.78 μl of 6.5% v/v DMS (Sigma-Aldrich) in 200 proof ethanol [(+)
581 channel] or with 200 proof ethanol [(-) channel]. The samples were incubated for 5 min at
582 37 °C. The DMS probing reaction was quenched by adding 6.67 μl of 14.5 μM 2-
583 mercaptoethanol and incubating the sample at 37 °C for 1 min. *In vitro* transcription
584 reactions were then quenched by addition of 250 μl of TRIzol reagent.
585
586 **RNA purification post-TECprobe-VL probing**
587
588 The RNA was purified from the quenched *in vitro* transcription reactions using the
589 following protocol. First, 50 μl of chloroform was added to the samples and the samples
590 were mixed by vortexing followed by centrifugation at 18,000*g* and 4 °C for 5 min. Next,
591 the aqueous layer was transferred to a new tube and nucleic acids were precipitated by
592 addition of 105 μl cold isopropanol and 1 μl GlycoBlue Coprecipitant (Invitrogen). The
593 samples were incubated at room temperature for 15 min and centrifuged at 18,000*g* and
594 4 °C for 15 min. The supernatant was discarded and the pellet containing the precipitated
595 nucleic acids was washed by addition of 200 μl 70% ethanol. Following the 70% ethanol
596 wash, the samples were centrifuged at 18,000*g* and 4 °C for 2 min and the supernatant
597 was discarded. The pelleted nucleic acids were resuspended in 25 μl of 1x DNase buffer
598 (10 mM Tris-Cl, pH 7.5, 2.5 mM $MgCl_2$) and mixed with 0.75 μl of Turbo DNase
599 (Invitrogen) to remove residual DNA template. The samples were incubated at 37 °C for
600 15 min and DNase digestion was quenched by addition of 250 μl TRIzol reagent
601 (Invitrogen). A second TRIzol extraction was performed as described above, except the
602 pellet containing the DMS-modified RNA transcripts was resuspended in 5 μl of 10% (v/v)
603 DMSO.
604
605 **RNA 3' adapter ligation onto the TECprobe-VL purified transcripts**
606 The 9N_VRA3 adapter oligonucleotide (0139, Supplementary Table 2) was pre-
607 adenylated with the 5' DNA Adenylation Kit (New England Biolabs) using the following
608 protocol. A 100 μl master mix was prepared that consisted of the 1X DNA Adenylation
609 Buffer (New England Biolabs), 100 μM ATP, 5 μM 9N_VRA3 oligo, and 5 μM Mth RNA
610 Ligase (New England Biolabs). The 100 μl master mix was split into 4 aliquots (25 μl
611 each) in PCR tubes and incubated in a thermal cycler set to 65 °C for 1 h. To clean up
612 the adenylation reactions, reactions were pooled to 50 μl followed by addition of 500 μl
613 TRIzol (Invitrogen) and 100 μl of chloroform to each 50 μl pool. The samples were

614 vortexed to mix and centrifuged at 18,000*g* and 4 °C for 5 min. The aqueous phase was
615 transferred to a new tube and the adapter was ethanol precipitated. The pellet was
616 resuspended in Tris-Cl, pH 8.0, and its concentration was quantified with the Qubit ssDNA
617 Assay Kit (Invitrogen) and a Qubit 3 Fluorometer. The pre-adenylated adapter was diluted
618 to 1 μM, divided into small aliquots, and stored at -20 °C.
619
620 The RNA 3' adapter ligation reactions were performed using the following protocol.
621 Purified RNA redissolved in 5 μl of 10% (v/v) DMSO was combined with 1x T4 RNA Ligase
622 Buffer (New England Biolabs), 0.5 U/μl SuperaseIN (Invitrogen), 0.05 μM pre-adenylated
623 9N_VRA3 adapter, 15 % PEG 8000, and 5 U/μl T4 RNA Ligase 2, truncated KQ (New
624 England Biolabs). The final volume for the ligation reactions was 20 μl and the reactions
625 were incubated at 25 °C for 2 h.
626
627 **SPRI bead purification of adapter-ligated RNA**
628
629 A solid-phase reversible immobilization (SPRI) bead purification protocol was used to
630 deplete excess 9N_VRA3 adapter oligonucleotide. The SPRI beads were prepared with
631 SpeedBead Magnetic Carboxylate Beads (Cytiva) using the protocol from Jolivet and
632 Foley[50]. The ligation reactions were combined with 17.5 μl of water, 40 μl anhydrous
633 isopropanol, and 22.5 μl of the SPRI beads. The samples were vortexed and incubated
634 at room temperature for 5 min. The samples were then placed on a magnetic separation
635 rack and the beads collected on the tube wall before disposing of the supernatant.
636 Keeping the tubes on the magnetic stand, the beads were washed twice with 200 μl of
637 70% ethanol. After discarding the second ethanol wash, the tubes were placed in a dry
638 bath set to 37 °C to evaporate the residual ethanol. The beads were resuspended in 25
639 μl of elution buffer (20 mM Tris-Cl pH 8.0, 50 mM KCl, 1 mM DTT, 0.1 mM EDTA, 0.1%
640 Triton X-100, 10 mM $MgCl_2$) and the samples were incubated for 3 minutes at room
641 temperature to elute the RNA. The samples were placed on a magnetic rack and beads
642 collected on the tube wall before aliquoting the supernatant containing the RNA into a
643 fresh tube.
644
645 **TECprobe-VL cDNA synthesis and cleanup**
646
647 The reverse transcription reactions were performed via capture of RNA transcripts on
648 streptavidin beads using a 5' biotinylated reverse transcription primer (0159,
649 Supplementary table 2), which anneals to the 9N_VRA3 sequence that was appended to
650 the intermediate riboswitch transcripts. Dynabeads MyOne Streptavidin C1 beads
651 (Invitrogen) were equilibrated as described previously[27]. 5 μl of 500 nM RT primer was
652 combined with the purified RNA samples and annealed in a thermal cycler using the
653 following program: 70 °C for 5 min, ramp to 50 °C at 0.1 °C /s, 50 °C for 5 min, ramp to
654 40 °C at 0.1 °C /s, 40 °C for 5 min, cool to 25 °C. The equilibrated streptavidin beads were
655 placed on a magnetic stand to allow the beads to collect on the tube wall and the
656 supernatant was discarded. The streptavidin beads were then resuspended with the
657 samples containing RNA annealed to the 5' biotinylated RT primer and incubated at room

658 temperature for 15 min on an end-over-end rotator. The samples were placed on a
659 magnetic stand and the beads were allowed to collect on the tube wall before discarding
660 the supernatant. The beads were resuspended in 19.5 μl of reverse transcription master
661 mix and incubated in a thermal cycler set to 42 °C for 2 min before addition of the reverse
662 transcriptase. Upon addition of 0.5 μl of SuperScript II Reverse Transcriptase (Invitrogen)
663 to each sample, the 20 μl RT reactions contained 1x first strand buffer (50 mM Tris-Cl,
664 pH 8.0, 75 mM KCl), 500 μM dNTPs, 10 mM DTT, 2 % formamide, 10 ng/μl Extreme
665 Thermostable Single-Stranded DNA Binding Protein (ET SSB) (New England Biolabs),
666 0.1 % Triton-X-100, and 3 mM $MnCl_2$. The reverse transcription reactions were incubated
667 at 42 °C for 180 min followed by a 70 °C incubation for 50 min to inactivate the SuperScript
668 II and then cooled to 12 °C. Next, the RNAs were degraded by adding 1.25 U RNase H
669 (New England Biolabs) and 12.5 U RNase I_f (New England Biolabs) to each sample and
670 the samples were incubated at 37 °C for 20 min followed by a 70 °C incubation for 20 min
671 to inactivate the RNases. The samples were placed on a magnetic stand and the beads
672 were allowed to collect on the tube wall. The supernatant was discarded and the beads
673 were resuspended in 75 μl of Tris Wash Buffer (10 mM Tris-Cl, pH 8.0, 0.05% Triton X-
674 100) to wash the beads. The samples were placed on a magnetic stand and the wash
675 was discarded. The bead-bound cDNA was resuspended in 25 μl of the Tris Wash Buffer
676 and stored at -20 °C.
677
678 **Chemical probing of equilibrium-refolded intermediate transcripts**
679
680 Single-round *in vitro* transcription using randomly biotinylated DNA templates was
681 executed as described for TECprobe-VL experiments above. To quench transcription,
682 600 μl of TRIzol was added to the reactions. Next, 120 μl of chloroform was added to the
683 samples and the samples were vortexed to mix followed by centrifugation at 18,000*g* and
684 4 °C for 5 min. The aqueous layer was transferred into a new tube and nucleic acids were
685 isopropanol precipitated as described for TECprobe-VL experiments except a larger
686 volume of isopropanol was used to account for the larger sample volume. The pellets
687 containing the intermediate RNA transcripts were resuspended in 30 μl of 1x TECprobe
688 transcription buffer (100 mM Tris-Cl, pH 7.2 or 8.5, 50 mM KCl, 1 mM DTT), placed on a
689 heat block set to 95 °C for 2 min, and snap-cooled on ice for 1 min. To each sample, 30
690 μl of 2x equilibration buffer (200 mM Tris-Cl, pH 7.2 or 8.5, 100 mM KCl, 2 mM DTT, 20
691 mM $MgCl_2$) was added, which contained either no Mn or 2 mM $MnCl_2$ (1 mM final in 60 μl
692 reaction), and the samples were incubated at 37 °C for 20 min. The RNAs were then
693 probed with DMS as described for TECprobe-VL experiments, and the DMS-probed RNA
694 was purified as described for TECprobe-VL experiments.
695
696 **Preparation of TECprobe-VL dsDNA libraries for sequencing**
697
698 cDNA libraries were PCR-amplified for high throughput sequencing using the following
699 protocol. Separate PCR reactions were performed for the (+) and (-) samples, which
700 contained 1x Q5 Reaction Buffer, 1x Q5 GC Enhancer, 200 μM dNTPs, 250 nM RPI
701 Indexing Primer (0163-0178,0235-0248, Supplementary table 2), 250 nM

dRP1_NoMod.R reverse primer (0162, Supplementary Table 2), 10 nM SC1Brdg_MINUS or SC1Brdg_PLUS channel barcode oligo (0160,0161, Supplementary Table 2), 12 μl of bead-bound cDNA library, and 0.02 U/μl Q5 High-Fidelity DNA Polymerase (New England Biolabs). Amplification was performed with the following thermal cycler program: 98 °C for 30 s, [98 °C for 10s, 62 °C for 20 s, 72 °C for 20s] x 22 cycles, 72 °C for 2 min, hold at 12 °C.

High-throughput DNA sequencing of TECprobe-VL libraries

Sequencing of the TECprobe-VL and equilibrium refolded intermediate transcript libraries was performed by Novogene Co. on a Novaseq X Plus system with 2 x 150 Paired End (PE) reads and a 20% PhiX spike in. The TECprobe-VL and equilibrium refolded intermediate transcript libraries were sequenced at a depth of ~30-60 million PE reads.

Sequencing of TECprobe-SL libraries was performed by Novogene Co. on a Novaseq X Plus system with 2 x 150 PE reads. No PhiX spike in was added since these libraries were sequenced in a partial lane. The TECprobe-SL libraries were sequenced at a depth of ~10 million PE reads.

TECprobe-VL data processing and visualization

Sequence read pre-processing, target generation using cotrans_preprocessor, and shapemapper2 run script generation were performed exactly as described in the published protocol using the publicly available TECprobe data processing tools (https://github.com/e-strobel-lab/TECtools). TECprobe visualization tools was used to assemble reactivity matrices and analyze the correlation between replicate data sets (https://github.com/e-strobel-lab/TECprobe_visualization). The compile_sm2_output script was used to assemble the reactivity profiles for intermediate transcripts into matrix format and to normalize the dataset. The normalized reactivity matrices were visualized in heatmap format using GraphPad Prism.

For the *alx* riboswitch, replicate data sets were required to obtain adequate sequencing depth for longer transcripts, as there was a strong bias in representation towards shorter transcripts for the amplified cDNA libraries. Plots with fraction of aligned reads per transcript length and alignment rates for *alx* co-transcriptional TECprobe-VL experiments are presented in SI Fig. 21. Additionally, the presence of two intrinsic termination sites in the *alx* riboswitch sequence (110 and 190 nt) results in a clear drop in sequencing depth for intermediate transcripts past these sites (SI Fig. 19A). For the co-transcriptional DMS-MaP libraries, 5-7 independent replicates were pooled per chemical probing condition to increase data quality for longer transcript lengths (see SI Figs 22-25 for individual and concatenated heatmaps). Plots with fraction of aligned reads per transcript length and alignment rates for *alx* equilibrium refolded TECprobe-VL experiments are presented in SI Fig. 26. For the equilibrium refolded *alx* TECprobe-VL experiments, 2 independent replicates were pooled per chemical probing condition to increase data quality for longer

746 transcript lengths (see SI Figs 27-30 for individual and concatenated heatmaps). To
747 further increase sequencing depth when necessary, multiple independent PCR
748 amplifications were performed with the same cDNA library and sequenced; reads were
749 subsequently pooled together for data processing.
750
751 For the *mntP* riboswitch, two replicate data sets were concatenated and analyzed
752 together after assessing the correlation between replicates using the
753 plot_cotrans_correlation script available in TECprobe visualization tools. Plots with
754 fraction of aligned reads per transcript length and alignment rates for co-transcriptional
755 *mntP* TECprobe-VL experiments are presented in SI Fig. 31 Plots with fraction of aligned
756 reads per transcript length and alignment rates for equilibrium refolded *mntP* TECprobe-
757 VL experiments are presented in SI Fig. 32. To further increase sequencing depth when
758 necessary, multiple independent PCR amplifications were performed with the same cDNA
759 library and sequenced; reads were subsequently pooled together for data processing.
760
761
762 ***In vitro* synthesis of full-length riboswitch RNAs with T7 RNAP and cleanup for**
763 **SHAPE-MaP and DMS-MaP**
764
765 RNA for *in vitro* SHAPE/DMS-MaP was synthesized using the HiScribe T7 High Yield
766 RNA Kit (New England Biolabs). 100 μL reactions were assembled according to
767 manufacturer instructions and incubated at 37 °C overnight. RNA was purified and
768 concentrated using the RNA Clean and Concentrator kit (Zymo Research). For the *alx*
769 riboswitch and *alx* aptamer, RNAs were gel-purified to isolate full-length transcripts away
770 from premature transcription termination products using a denaturing PAGE (8%
771 acrylamide, 8 M urea, 0.5x TBE (Fisher Scientific)). For gel-purification, RNAs were
772 diluted 1:5 in buffer and mixed with an equal volume 2x formamide loading dye (95%
773 formamide, 0.5 mM EDTA, 0.025% bromophenol blue, 0.025% xylene cyanol), heated at
774 95 °C for 2 mins, and loaded on a pre-heated gel. Gel was run at 50 W, stained with 1x
775 SYBR Green II RNA Gel Stain (Invitrogen) in 1X TBE for 10 mins, and visualized using a
776 Edvotek TruBlu 2 Blue Transilluminator. Bands corresponding to full-length RNA were
777 excised and eluted in 10 mL TE buffer (10 mM Tris pH 8.0, 1 mM EDTA pH 8.0) at 4 °C
778 overnight. The eluted solution of RNA was spun to pellet acrylamide, and RNA was
779 concentrated using an Amicon Ultra Centrifugal filter (3 kDa molecular weight cutoff).
780 RNAs were ethanol precipitated, stored at -20 °C, and resuspended in RNase-free H_2O.
781 For the *mntP* riboswitch, there are no terminated transcripts, eliminating the need for gel
782 purification. After transcription and cleanup, *mntP* RNAs were ethanol precipitated, stored
783 at -20 °C, and resuspended in RNase free H_2O.
784
785 **SHAPE-MaP and DMS-MaP on the full-length equilibrium refolded *alx* and *mntP***
786 **riboswitches**
787 5 pmol of RNA in added RNase-free H_2O to a volume of 6 μL was heat denatured for 2
788 mins at 95 °C, cooled at 4 °C for 2 mins, and then 3 μL buffer was added for a final volume
789 of 9 μL. The final buffer concentration was 100 mM HEPES, 100 mM NaCl, and 5 mM

790 $MgCl_2$ at either pH 7.2 or pH 8.4 and supplemented with 1 mM $MnCl_2$ where indicated.
791 RNA was incubated at 37 °C for 20 mins to allow refolding. For modification with 1M7, 9
792 μL of RNA was mixed with 1 μL of 100 mM 1M7 ("+" modified sample) or 1 μL DMSO ("-
793 " negative control), incubated for 75 s at 37 °C, and placed on ice. For the denatured
794 control, 5 pmol RNA (3 μL) was mixed with 5 μL formamide and 1 μL 10x denaturing
795 buffer (500 mM HEPES, 40 mM EDTA) at pH 7.2 or 8.4. RNA was denatured for 1 min at
796 95 °C, mixed with 1 μL of 100 mM 1M7, incubated at 95 °C for 1 min, and placed on ice.
797 All RNAs were purified and eluted in 50 μL of RNase-free H_2O using MicroSpin G-25
798 columns (Cytiva) and stored at -20 °C. For modification with DMS, 9 μL of RNA was mixed
799 with 1 μL of 6.5% v/v DMS ("+" modified sample) or 1 μL ethanol ("-" negative control),
800 incubated for 5 minutes at 37 °C, quenched with 2.4 μL of 30% v/v 2-mercaptoethanol
801 solution at 37 °C for 1 min before placing on ice. For the denatured control, 5 pmol RNA
802 (3 μL) was mixed with 5 μL formamide and 1 μL 10x denaturing buffer (500 mM HEPES,
803 40 mM EDTA) at pH 7.2 or 8.4. Then RNA was denatured for 1 min at 95 °C, mixed with
804 1 μL of 6.5% v/v DMS, incubated at 95 °C for 1 min, quenched with 2.4 μL of 30% 2-
805 mercaptoethanol solution at 37 °C for 1 min before placing on ice. All RNAs were purified
806 and eluted in 50 μL of RNase-free H_2O using MicroSpin G-25 columns (Cytiva) and stored
807 at -20 °C.
808
809 Reverse transcription (RT) of 10 μL of RNA was performed by annealing 1 μL RT primer
810 (0277) for 5 min at 65 °C. Then, 8 μL RT buffer was added (50 mM Tris-Cl pH 8, 75 mM
811 KCl, 10 mM DTT, 0.5 mM dNTPs, and $MnCl_2$ added to 15 mM before use). Samples were
812 incubated for 2 min at 42 °C before introducing Superscript II reverse transcriptase
813 (Thermo Fisher Scientific). RT reactions were incubated for 3 h at 42 °C. The reverse
814 transcriptase was inactivated for 15 min at 70 °C before storing the reactions at 4 °C.
815 cDNA was purified and eluted in 50 μL of RNase-free H_2O using MicroSpin G-25 columns
816 (Cytiva) and stored at -20 °C. The first PCR (step 1) amplified cDNA through 20
817 amplification cycles using primers 0278 and 0279. Excess primer was removed using the
818 Monarch PCR & DNA Cleanup Kit (New England Biolabs). The second PCR (step 2)
819 further amplified the first PCR amplicon through an additional 10 cycles. The step 2 PCR
820 used primers 0149 and an RPI indexing primer (0163-0178 and 0235-0248). Step 2 PCR
821 was cleaned up using Agencourt AMPure XP beads (Beckman Coulter), and final DNA
822 concentration was measured using the Invitrogen Quant-IT dsDNA High-Sensitivity HS
823 Assay kit quantified with a BioTek Synergy H1 Multimode Microplate Reader before
824 pooling libraries for sequencing. Sequencing of these pooled libraries was performed by
825 Novogene Co. on a NovaSeq 6000 system with 100M 150 PE reads.
826
827 ***In vivo* DMS-MaP of the full-length *alx* riboswitch**
828
829 The plasmid pMIS518 was transformed into MC4100Δ*alx* cells, and a 5-mL culture was
830 grown at 37 °C overnight with shaking at 200 rpm. A 1:100 dilution of overnight culture
831 into 20 mL of fresh potassium-modified LB medium (LBK) media (LBK at pH 7.2 or 8.4

832 and with supplemented $MnCl_2$ where indicated) was grown at 37 °C with shaking at 200
833 rpm to an optical density of 0.3-0.5 at 600 nm (OD_{600}). The LBK was prepared by replacing
834 NaCl with equimolar KCl, and was buffered with 100 mM N-[Tris(hydroxymethyl)methyl]-
835 3-amino propane sulfonic acid (TAPS) and pH adjusted with KOH to 8.4 for the alkaline
836 medium. For the DMS-probed sample, 10 mL of culture was exposed to 10 μL of ≥99.5%
837 DMS (Sigma-Aldrich), shaken at 200 rpm at 30 °C for 5 min, and quenched with 1.6 mL
838 of 0.6 M 2-mercaptoethanol. For the untreated sample, 10 mL of culture was shaken at
839 200 rpm at 30 °C for 5 min, and quenched with 1.6 mL of 0.6 M 2-mercaptoethanol. The
840 cultures were spun at 4 °C and the pellets were resuspended in 0.6 mL of hot total RNA
841 lysis buffer pre-heated to 60 °C (1 mM EDTA, 20 mM Na acetate pH 5.5, and 0.5% SDS).
842 The sample was phenol-chloroform extracted twice, followed by two chloroform
843 extractions and ethanol precipitation. The pellet was then resuspended in 100 μL RNase-
844 free H_2O, treated with 10 U Turbo DNase for 1 h at 37 °C, and again phenol-chloroform
845 extracted, followed by chloroform extraction, ethanol precipitation, and pellets were
846 resuspended in 100 μL RNase-free H_2O. 0.5 μL purified total RNA was used for RT, and
847 all subsequent library preparation steps were identical to the above *in vitro* DMS-MaP
848 protocol.
849
850 **RNA structure prediction and visualization**
851
852 RNA structure prediction for co-transcriptionally probed riboswitch folding intermediates
853 was performed using the RNAstructure V6.4[51] Fold command with default settings,
854 adding the DMS outputs as a constraint, and forcing the 3'-most 11 to 14 nt to be single-
855 stranded to account for the *E. coli* RNAP footprint. The set of minimum free-energy
856 structures were visualized in VARNA[52] to assess agreement with the DMS probing data,
857 and structure diagrams were colored in accordance with DMS reactivity. Additionally,
858 existing X-ray crystal structures for Mn-sensing aptamer domains were visualized with
859 UCSF Chimera[53] and used to guide modeling of conserved secondary and tertiary
860 structure motifs within the *alx* and *mntP* aptamers. RNA structure prediction for
861 equilibrium refolded riboswitch folding intermediates was performed as described above;
862 however, the 3' most nt were not kept single-stranded since the intermediate RNA
863 transcripts were extracted from stalled transcription elongation complexes before DMS
864 probing.
865
866 The denatured and equilibrium-refolded full-length *mntP* riboswitch, *alx* riboswitch, and
867 *alx* aptamer RNA structures were predicted using the RNAStructure V6.4[51] Fold
868 command with default settings, adding the SHAPE or DMS outputs as a constraint. The
869 minimum free energy structures were visualized in VARNA[52] and colored in accordance
870 with nucleotide reactivity.
871
872
873
874

875 **β-galactosidase assays**
876
877 Overnight culture of each strain was diluted 1:100 into LBK with appropriate antibiotic at
878 either pH 6.8 or pH 8.4, with or without 1 mM supplemented $MnCl_2$. The cultures were
879 grown to mid-log phase and supplemented with 1 mM IPTG where necessary for
880 expression of T7 RNAP. β-galactosidase assays were performed using the Miller
881 method[54]. Briefly, bacterial growth was measured using OD_{600} before cultures were
882 placed on ice. 100 μL cells were lysed via vortexing in 900 μL sodium phosphate buffer
883 (100 mM sodium phosphate pH 7, 10 mM KCl, 2 mM $MgSO_4$, 38 mM 2-mercaptoethanol),
884 20 μL 0.1% SDS, and 20 μL chloroform. Substrate *O*-nitrophenyl-β-D-galactopyranoside
885 (ONPG) was added and the reaction was stopped with 1 M Na_2CO_3 when a yellow color
886 appeared, or after 35 min. After centrifuging 5 min at 16,000 g, absorbance was measured
887 at 420 nm (A_{420}) to calculate activity using Miller units. Each culture was tested in
888 duplicate and A_{420} values were averaged. Each final reported value is an average of three
889 replicates with standard deviation.
890
891 **Sequence analysis for *yybP-ykoY* riboswitches**
892
893 The sequences for *yybP-ykoY* riboswitches were downloaded from the Rfam database
894 (Rfam reference number RF00080) and aligned using the Kalign multi sequence
895 alignment program (https://www.ebi.ac.uk/jdispatcher/msa). The sequence alignment
896 and consensus L3 sequence was visualized using Jalview[55]. The *yybP-ykoY* riboswitch
897 sequences found within the Enterobacteriales order were accessed from both the Rfam
898 database and from *yybP-ykoY* regulog collection
899 (https://regprecise.lbl.gov/collection_rfam.jsp?riboswitch_id=13). These sequences were
900 aligned with the Muscle multi sequence alignment program
901 (https://www.ebi.ac.uk/jdispatcher/msa). The sequence alignment and consensus L3
902 sequence was visualized using Jalview[55].
903

904 **Data Availability**

905 The raw sequencing data generated in this study will be deposited into the Sequencing
906 Read Archive (https://www.ncbi.nlm.nih.gov/sra) with the BioProject accession code
907 PRJNA1197522. Individual BioSample accession codes will be provided in a
908 Supplementary Table. All processed reactivity data will be deposited in the RNA Mapping
909 Database (https://rmdb.stanford.edu/) and the individual accession codes will be provided
910 in a Supplementary Table.

911 **References**

912 1. Imlay, J. A. The Mismetallation of Enzymes during Oxidative Stress. *J. Biol. Chem.* **289**,
913 28121–28128 (2014).
914 2. Imlay, J. A. The molecular mechanisms and physiological consequences of oxidative
915 stress: lessons from a model bacterium. *Nat. Rev. Microbiol.* **11**, 443–454 (2013).
916 3. Chandrangsu, P., Rensing, C. & Helmann, J. D. Metal homeostasis and resistance in
917 bacteria. *Nat. Rev. Microbiol.* **15**, 338–350 (2017).
918 4. Lee, J.-W. & Helmann, J. D. Functional specialization within the Fur family of
919 metalloregulators. *BioMetals* **20**, 485–499 (2007).
920 5. Glasfeld, A., Guedon, E., Helmann, J. D. & Brennan, R. G. Structure of the manganese-
921 bound manganese transport regulator of *Bacillus subtilis*. *Nat. Struct. Mol. Biol.* **10**,
922 652–657 (2003).
923 6. Price, I. R., Gaballa, A., Ding, F., Helmann, J. D. & Ke, A. Mn^{2+}-Sensing Mechanisms of
924 *yybP-ykoY* Orphan Riboswitches. *Mol. Cell* **57**, 1110–1123 (2015).
925 7. Dann, C. E. *et al.* Structure and Mechanism of a Metal-Sensing Regulatory RNA. *Cell*
926 **130**, 878–892 (2007).
927 8. Furukawa, K. *et al.* Bacterial Riboswitches Cooperatively Bind Ni^{2+} or Co^{2+} Ions and
928 Control Expression of Heavy Metal Transporters. *Mol. Cell* **57**, 1088–1098 (2015).
929 9. Serganov, A. & Nudler, E. A Decade of Riboswitches. *Cell* **152**, 17–24 (2013).
930 10. Dambach, M. *et al.* The Ubiquitous *yybP-ykoY* Riboswitch Is a Manganese-Responsive
931 Regulatory Element. *Mol. Cell* **57**, 1099–1109 (2015).

932 11. Kavita, K. & Breaker, R. R. Discovering riboswitches: the past and the future. *Trends*
933 *Biochem. Sci.* **48**, 119–141 (2023).
934 12. Suddala, K. C. *et al.* Local-to-global signal transduction at the core of a Mn^{2+} sensing
935 riboswitch. *Nat. Commun.* **10**, 4304 (2019).
936 13. Sung, H.-L. & Nesbitt, D. J. Single-Molecule FRET Kinetics of the Mn^{2+} Riboswitch:
937 Evidence for Allosteric Mg^{2+} Control of "Induced-Fit" vs "Conformational Selection"
938 Folding Pathways. *J. Phys. Chem. B* **123**, 2005–2015 (2019).
939 14. Wickiser, J. K., Winkler, W. C., Breaker, R. R. & Crothers, D. M. The Speed of RNA
940 Transcription and Metabolite Binding Kinetics Operate an FMN Riboswitch. *Mol. Cell*
941 **18**, 49–60 (2005).
942 15. Chauvier, A. *et al.* Transcriptional pausing at the translation start site operates as a
943 critical checkpoint for riboswitch regulation. *Nat. Commun.* **8**, 13892 (2017).
944 16. Strobel, E. J., Cheng, L., Berman, K. E., Carlson, P. D. & Lucks, J. B. A ligand-gated strand
945 displacement mechanism for ZTP riboswitch transcription control. *Nat. Chem. Biol.* **15**,
946 1067–1076 (2019).
947 17. Chauvier, A., Dandpat, S. S., Romero, R. & Walter, N. G. A nascent riboswitch helix
948 orchestrates robust transcriptional regulation through signal integration. *Nat.*
949 *Commun.* **15**, 3955 (2024).
950 18. Nechooshtan, G., Elgrably-Weiss, M., Sheaffer, A., Westhof, E. & Altuvia, S. A pH-
951 responsive riboregulator. *Genes Dev.* **23**, 2650–2662 (2009).

952 19. Sharma, R. & Mishanina, T. V. A riboswitch-controlled TerC family transporter Alx tunes
953 intracellular manganese concentration in *Escherichia coli* at alkaline pH. *J. Bacteriol.*
954 **206**, e00168-24 (2024).
955 20. Zeinert, R. *et al.* Structure–function analysis of manganese exporter proteins across
956 bacteria. *J. Biol. Chem.* **293**, 5715–5730 (2018).
957 21. Bachas, S. T. & Ferré-D'Amaré, A. R. Convergent Use of Heptacoordination for Cation
958 Selectivity by RNA and Protein Metalloregulators. *Cell Chem. Biol.* **25**, 962-973.e5
959 (2018).
960 22. Adeolu, M., Alnajar, S., Naushad, S. & S. Gupta, R. Genome-based phylogeny and
961 taxonomy of the '*Enterobacteriales*': proposal for *Enterobacterales* ord. nov. divided
962 into the families *Enterobacteriaceae*, *Erwiniaceae* fam. nov., *Pectobacteriaceae* fam.
963 nov., *Yersiniaceae* fam. nov., *Hafniaceae* fam. nov., *Morganellaceae* fam. nov., and
964 *Budviciaceae* fam. nov. *Int. J. Syst. Evol. Microbiol.* **66**, 5575–5599 (2016).
965 23. Padan, E., Bibi, E., Ito, M. & Krulwich, T. A. Alkaline pH homeostasis in bacteria: New
966 insights. *Biochim. Biophys. Acta BBA - Biomembr.* **1717**, 67–88 (2005).
967 24. Hartmann, F. S. F. *et al.* Visualizing the pH in *Escherichia coli* Colonies via the Sensor
968 Protein mCherryEA Allows High-Throughput Screening of Mutant Libraries. *mSystems*
969 **7**, e00219-22 (2022).
970 25. Smola, M. J., Rice, G. M., Busan, S., Siegfried, N. A. & Weeks, K. M. Selective 2'-hydroxyl
971 acylation analyzed by primer extension and mutational profiling (SHAPE-MaP) for
972 direct, versatile and accurate RNA structure analysis. *Nat. Protoc.* **10**, 1643–1669
973 (2015).

974 26. Szyjka, C. E. & Strobel, E. J. Cotranscriptional RNA Chemical Probing. in *Riboregulator*
975 *Design and Analysis* (eds. Chappell, J. & Takahashi, M. K.) vol. 2518 291–330 (Springer
976 US, New York, NY, 2022).
977 27. Szyjka, C. E. & Strobel, E. J. Observation of coordinated RNA folding events by
978 systematic cotranscriptional RNA structure probing. *Nat. Commun.* **14**, 7839 (2023).
979 28. Stephen, C. & Mishanina, T. V. Alkaline pH has an unexpected effect on transcriptional
980 pausing during synthesis of the *Escherichia coli* pH-responsive riboswitch. *J. Biol.*
981 *Chem.* **298**, 102302 (2022).
982 29. Kaur, G. *et al.* Novel MntR-Independent Mechanism of Manganese Homeostasis in
983 *Escherichia coli* by the Ribosome-Associated Protein HflX. *J. Bacteriol.* **196**, 2587–2597
984 (2014).
985 30. Kaur, G. *et al.* Affected energy metabolism under manganese stress governs cellular
986 toxicity. *Sci. Rep.* **7**, 11645 (2017).
987 31. Martin, J. E., Waters, L. S., Storz, G. & Imlay, J. A. The *Escherichia coli* Small Protein
988 MntS and Exporter MntP Optimize the Intracellular Concentration of Manganese. *PLOS*
989 *Genet.* **11**, e1004977 (2015).
990 32. Siegfried, N. A., Busan, S., Rice, G. M., Nelson, J. A. E. & Weeks, K. M. RNA motif
991 discovery by SHAPE and mutational profiling (SHAPE-MaP). *Nat. Methods* **11**, 959–965
992 (2014).
993 33. Papp-Wallace, K. M. & Maguire, M. E. Magnesium Transport and Magnesium
994 Homeostasis. *EcoSal Plus* **3**, 10.1128/ecosalplus.5.4.4.2 (2008).

995 34. Anand, V. S. & Patel, S. S. Transient State Kinetics of Transcription Elongation by T7 RNA
996 Polymerase. *J. Biol. Chem.* **281**, 35677–35685 (2006).
997 35. Wang, M. D. *et al.* Force and Velocity Measured for Single Molecules of RNA
998 Polymerase. *Science* **282**, 902–907 (1998).
999 36. Balint, E. & Unk, I. For the Better or for the Worse? The Effect of Manganese on the
1000 Activity of Eukaryotic DNA Polymerases. *Int. J. Mol. Sci.* **25**, 363 (2023).
1001 37. Zubradt, M. *et al.* DMS-MaPseq for genome-wide or targeted RNA structure probing in
1002 vivo. *Nat. Methods* **14**, 75–82 (2017).
1003 38. Mustoe, A. M., Lama, N. N., Irving, P. S., Olson, S. W. & Weeks, K. M. RNA base-pairing
1004 complexity in living cells visualized by correlated chemical probing. *Proc. Natl. Acad.*
1005 *Sci.* **116**, 24574–24582 (2019).
1006 39. Nechooshtan, G., Elgrably-Weiss, M. & Altuvia, S. Changes in transcriptional pausing
1007 modify the folding dynamics of the pH-responsive RNA element. *Nucleic Acids Res.* **42**,
1008 622–630 (2014).
1009 40. Saenger, W. *Principles of Nucleic Acid Structure*. (Springer New York, New York, NY,
1010 1984). doi:10.1007/978-1-4612-5190-3.
1011 41. Liberman, J. A. *et al.* Structural analysis of a class III preQ$_1$ riboswitch reveals an
1012 aptamer distant from a ribosome-binding site regulated by fast dynamics. *Proc. Natl.*
1013 *Acad. Sci.* **112**, (2015).
1014 42. Jones, C. P. & Ferré-D'Amaré, A. R. Recognition of the bacterial alarmone ZMP through
1015 long-distance association of two RNA subdomains. *Nat. Struct. Mol. Biol.* **22**, 679–685
1016 (2015).

1017 43. Peselis, A. & Serganov, A. *ykkC* riboswitches employ an add-on helix to adjust
1018 specificity for polyanionic ligands. *Nat. Chem. Biol.* **14**, 887–894 (2018).
1019 44. Ren, A., Rajashankar, K. R. & Patel, D. J. Fluoride ion encapsulation by Mg^{2+} ions and
1020 phosphates in a fluoride riboswitch. *Nature* **486**, 85–89 (2012).
1021 45. Morgan, J. J. Kinetics of reaction between O_2 and Mn(II) species in aqueous solutions.
1022 *Geochim. Cosmochim. Acta* **69**, 35–48 (2005).
1023 46. Hu, S. *et al.* Hematite-mediated Mn(II) abiotic oxidation under oxic conditions: pH
1024 effect and mineralization. *J. Colloid Interface Sci.* **636**, 267–278 (2023).
1025 47. Spicuglia, S., Kumar, S., Chasson, L., Payet-Bornet, D. & Ferrier, P. Potassium
1026 permanganate as a probe to map DNA–protein interactions *in vivo*. *J. Biochem.*
1027 *Biophys. Methods* **59**, 189–194 (2004).
1028 48. Davis, C. A., Bingman, C. A., Landick, R., Record, M. T. & Saecker, R. M. Real-time
1029 footprinting of DNA in the first kinetically significant intermediate in open complex
1030 formation by *Escherichia coli* RNA polymerase. *Proc. Natl. Acad. Sci.* **104**, 7833–7838
1031 (2007).
1032 49. Saba, J. *et al.* The elemental mechanism of transcriptional pausing. *eLife* **8**, e40981
1033 (2019).
1034 50. Jolivet, P. & Foley,J. SPRI bead mix. *protocols.io* (2020) doi:https://doi.org/10.
1035 17504/protocols.io.bnz4mf8w.
1036 51. Reuter, J. S. & Mathews, D. H. RNAstructure: software for RNA secondary structure
1037 prediction and analysis. *BMC Bioinformatics* **11**, 129 (2010).

52. Darty, K., Denise, A. & Ponty, Y. VARNA: Interactive drawing and editing of the RNA secondary structure. *Bioinformatics* **25**, 1974–1975 (2009).

53. Pettersen, E. F. *et al.* UCSF Chimera—A visualization system for exploratory research and analysis. *J. Comput. Chem.* **25**, 1605–1612 (2004).

54. Miller, JH. *A Short Course in Bacterial Genetics: A Laboratory Manual and Handbook for Escherichia Coli and Related Bacteria*. (Cold Spring Harbor Laboratory, Cold Spring Harbor, NY, 1992).

55. Waterhouse, A. M., Procter, J. B., Martin, D. M. A., Clamp, M. & Barton, G. J. Jalview Version 2—a multiple sequence alignment editor and analysis workbench. *Bioinformatics* **25**, 1189–1191 (2009).

1060 **Figures**

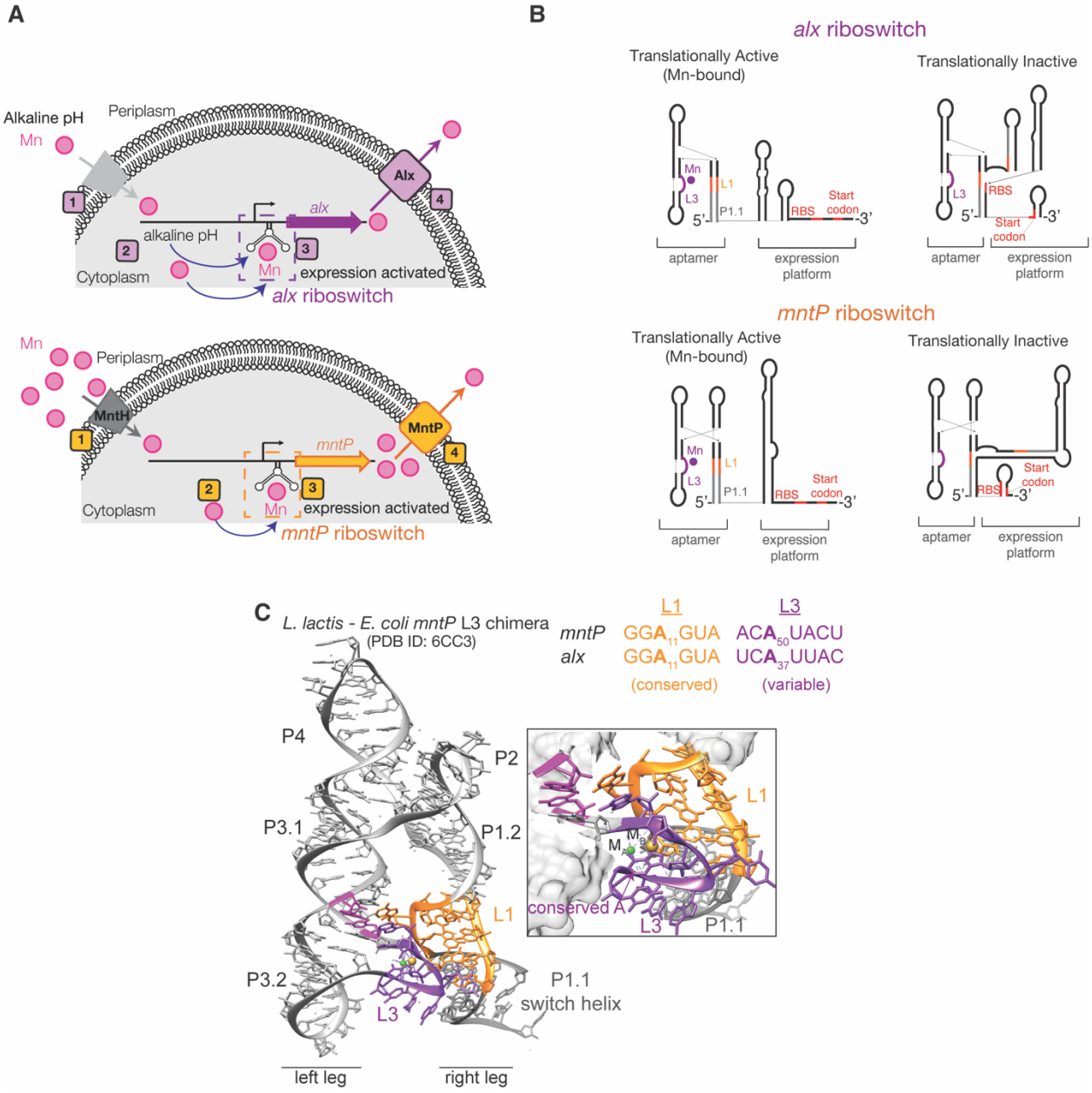

1061
1062
1063
1064 **Figure 1. Introduction to the *E. coli alx* and *mntP* Mn-sensing translational**
1065 **riboswitches. A.** Cartoon model of *alx* and *mntP* riboregulation of their respective genes
1066 in *E. coli*. (Top panel) At alkaline pH, the cytosolic [Mn] increases in *E. coli*, resulting in
1067 the *alx* riboswitch turning "on" expression of Alx, an Mn exporter. (Bottom panel) An
1068 increase in environmental [Mn] results in the *mntP* riboswitch turning "on" expression of
1069 MntP, the major Mn exporter in *E. coli*. **B.** Cartoon models of the *alx* and *mntP*
1070 riboswitches in their translationally active vs. inactive conformations. L3 (purple), L1
1071 (orange), P1.1 (gray), and RBS/start codon (red) are highlighted. **C.** *L. lactis* Mn-sensing

1072 aptamer crystal structure with the *E. coli mntP* L3 sequence (PDB 1D: 6CC3). “Left leg”
1073 and “right leg” refer to coaxially stacked helices in the aptamer. L3 (purple), L1 (orange),
1074 P1.1 (gray), and G-C receptor base pair in cross-helix A-minor (magenta) are highlighted.
1075 Mg^{2+} in the M_A site and Cd^{2+} in the M_B site (captured instead of Mn^{2+}) are green and
1076 yellow spheres, respectively. Sequence alignment of *alx* and *mntP* L1 and L3 are orange
1077 and yellow, respectively.
1078

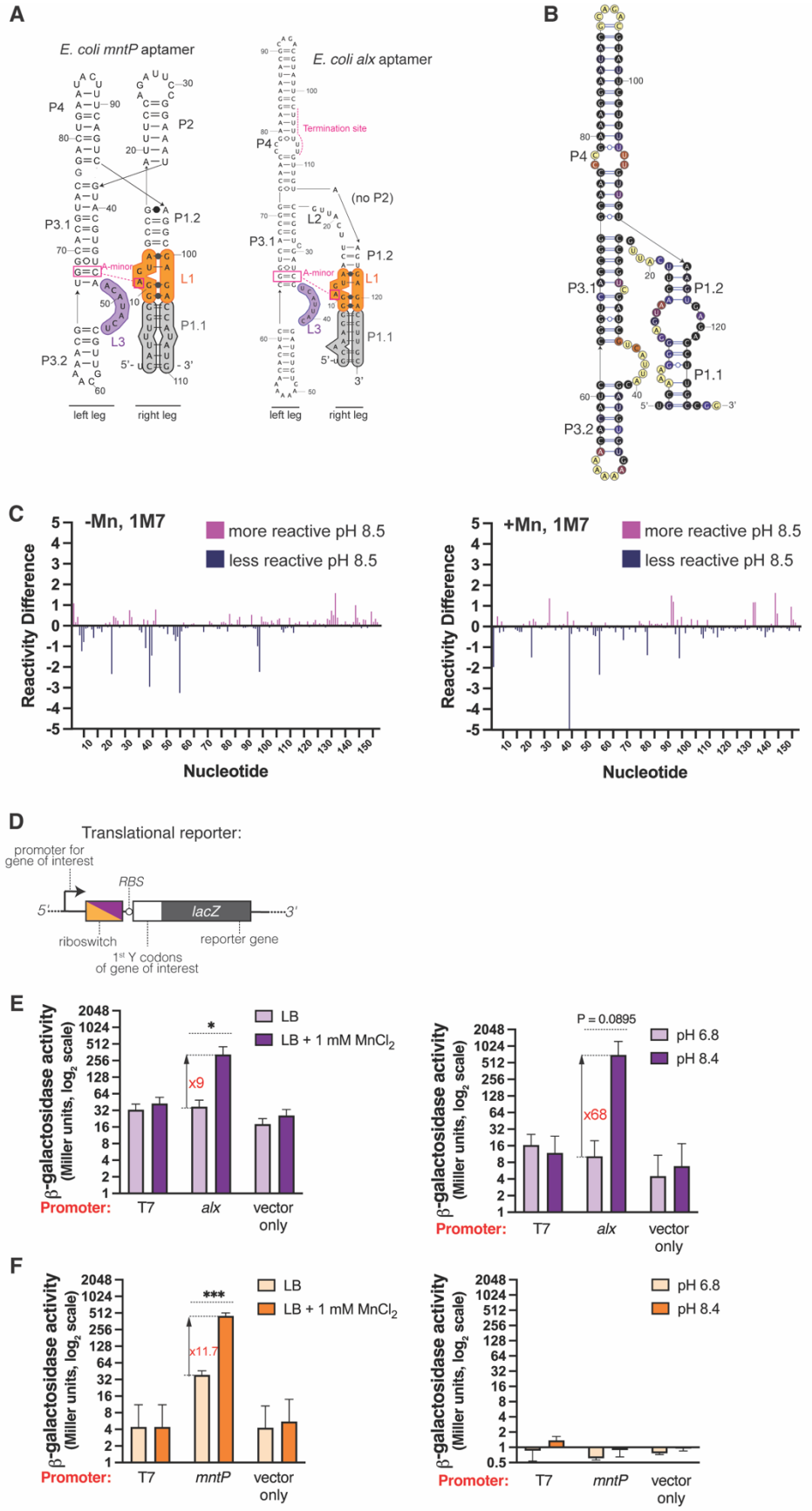
A
E. coli mntP aptamer
E. coli alx aptamer
Termination site
(no P2)
A-minor
L1
L2
L3
P1.1
P1.2
P2
P3.1
P3.2
P4
left leg
right leg
B
C
-Mn, 1M7
+Mn, 1M7
more reactive pH 8.5
less reactive pH 8.5
Reactivity Difference
Nucleotide
D
Translational reporter:
promoter for gene of interest
RBS
lacZ
5'
3'
riboswitch
reporter gene
1st Y codons of gene of interest
E
β-galactosidase activity (Miller units, log2 scale)
LB
LB + 1 mM MnCl2
x9
x68
P = 0.0895
pH 6.8
pH 8.4
Promoter:
T7
alx
vector only
F
x11.7
mntP
1079

Figure 2. Aptamer architectures and riboswitch-controlled translational response *in vivo*. A. *mntP* and *alx* aptamer structure models showing the *mntP* 4WJ and *alx* 3WJ elements. The key Mn-sensing loops (L1 is orange and L3 is purple) and the P1.1 switch helix (gray) are highlighted. **B.** Secondary structure model of equilibrium-refolded (pH 7.2 –Mn) *alx* aptamer modeled based on reactivity with 1M7. **C.** Individual nucleotide reactivity differences when modified with 1M7 at neutral (7.2) vs alkaline pH (8.5), measured in the presence or absence of Mn. **D.** Translational reporter construct design for *alx* and *mntP* translational reporters with the native or T7 promoter. **E.** Translational response of *alx* to supplemented Mn (left) or alkaline pH (right) as a function of promoter. Statistical analysis done using a parametric unpaired t-test to assess significance. **F.** Translational response of *mntP* to supplemented Mn (left) or alkaline pH (right) as a function of promoter. Statistical analysis done using a parametric unpaired t-test to assess significance.

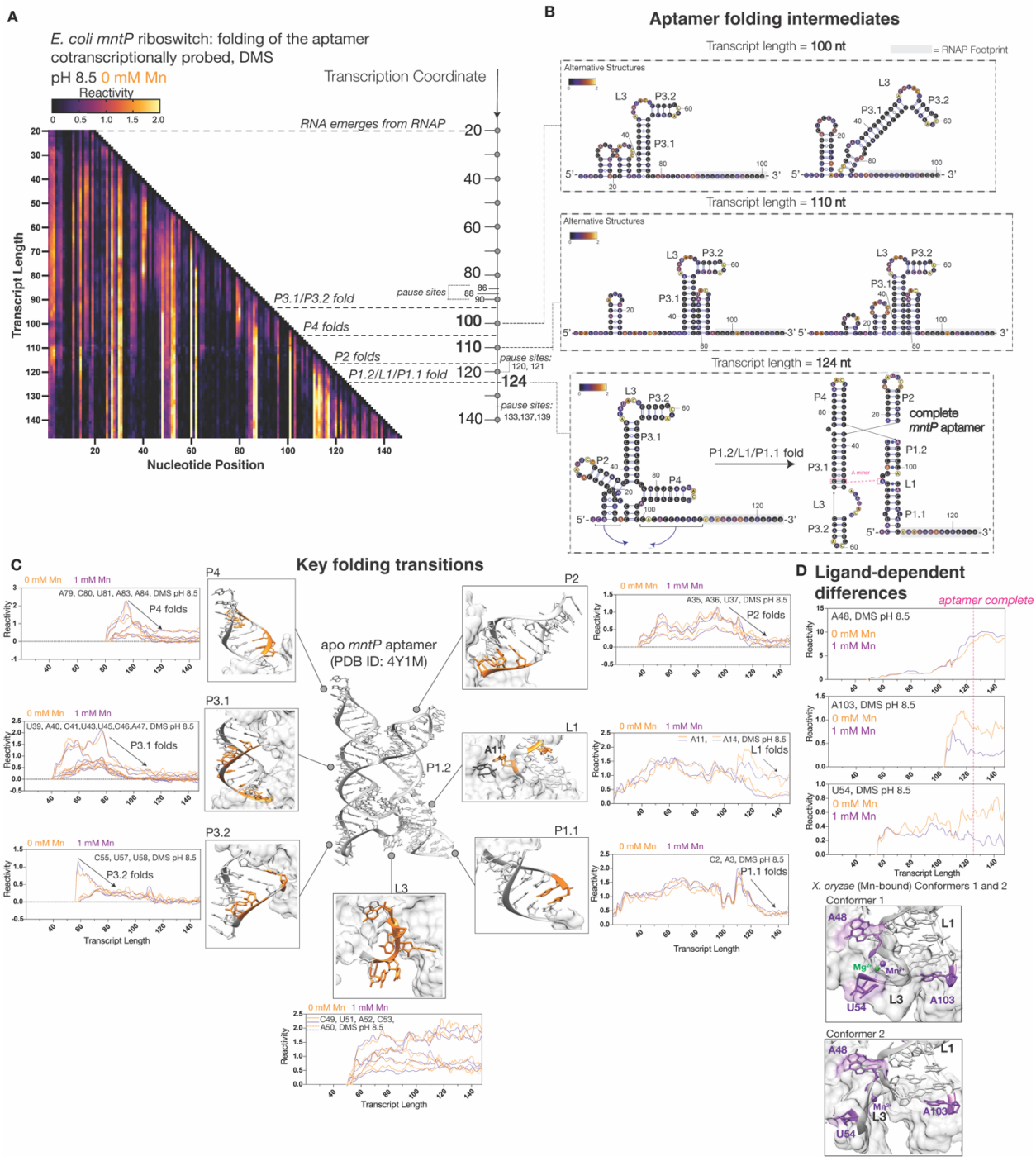
A
E. coli mntP riboswitch: folding of the aptamer cotranscriptionally probed, DMS
pH 8.5 0 mM Mn
Reactivity
Transcription Coordinate
RNA emerges from RNAP
P3.1/P3.2 fold
P4 folds
P2 folds
P1.2/L1/P1.1 fold
pause sites
pause sites: 120, 121
pause sites: 133,137,139
Transcript Length
Nucleotide Position
B
Aptamer folding intermediates
Transcript length = 100 nt
= RNAP Footprint
Alternative Structures
Transcript length = 110 nt
Transcript length = 124 nt
P1.2/L1/P1.1 fold
complete mntP aptamer
C
Key folding transitions
0 mM Mn 1 mM Mn
A79, C80, U81, A83, A84, DMS pH 8.5
P4 folds
U39, A40, C41,U43,U45,C46,A47, DMS pH 8.5
P3.1 folds
C55, U57, U58, DMS pH 8.5
P3.2 folds
apo mntP aptamer (PDB ID: 4Y1M)
A35, A36, U37, DMS pH 8.5
P2 folds
A11, A14, DMS pH 8.5
L1 folds
C2, A3, DMS pH 8.5
P1.1 folds
C49, U51, A52, C53, A50, DMS pH 8.5
Reactivity
Transcript Length
D Ligand-dependent differences
aptamer complete
A48, DMS pH 8.5
A103, DMS pH 8.5
U54, DMS pH 8.5
X. oryzae (Mn-bound) Conformers 1 and 2
Conformer 1
Conformer 2

Figure 3. Co-transcriptional DMS probing of the *mntP* riboswitch aptamer at alkaline pH. A. TECprobe-VL DMS reactivity matrix for the *mntP* aptamer at pH 8.5. Reactivities shown were normalized with a single, whole-dataset calculated normalization factor. Data are from two independent replicates that were concatenated and analyzed together. **B.** Secondary structures of *mntP* aptamer folding intermediates colored by DMS reactivity of the indicated transcript at pH 8.5. **C.** Transcript length-dependent reactivity changes showing folding transitions of the *mntP* aptamer at pH 8.5 ± 1 mM Mn. DMS data for 0 mM Mn (orange) and 1 mM Mn (purple) conditions from Fig. 3A and SI Fig. 3, respectively. *E. coli mntP* apo aptamer (PDB ID: 4Y1M) shown with labeled loops and helical domains. Nt highlighted in orange correspond to the nt positions with reactivities plotted in the adjacent graph. **D.** Plots show transcript length- and Mn-dependent reactivity changes in *mntP* aptamer folding intermediates at pH 8.5 ± 1 mM Mn. DMS data for 0 mM Mn (orange) and 1 mM Mn (purple) conditions from Fig. 3A and SI Fig. 3, respectively. Vertical dotted line marks completion of aptamer folding. *X. oryzae* aptamer metal-sensing core (PDB ID: 6N2V) with Mg^{2+} (green sphere) and Mn^{2+} (purple sphere) highlighted. Conformer 1 shows Mn^{2+} fully bound and Conformer 2 shows Mn^{2+} partially bound. Nt highlighted in purple correspond to nt reactivity plots above.

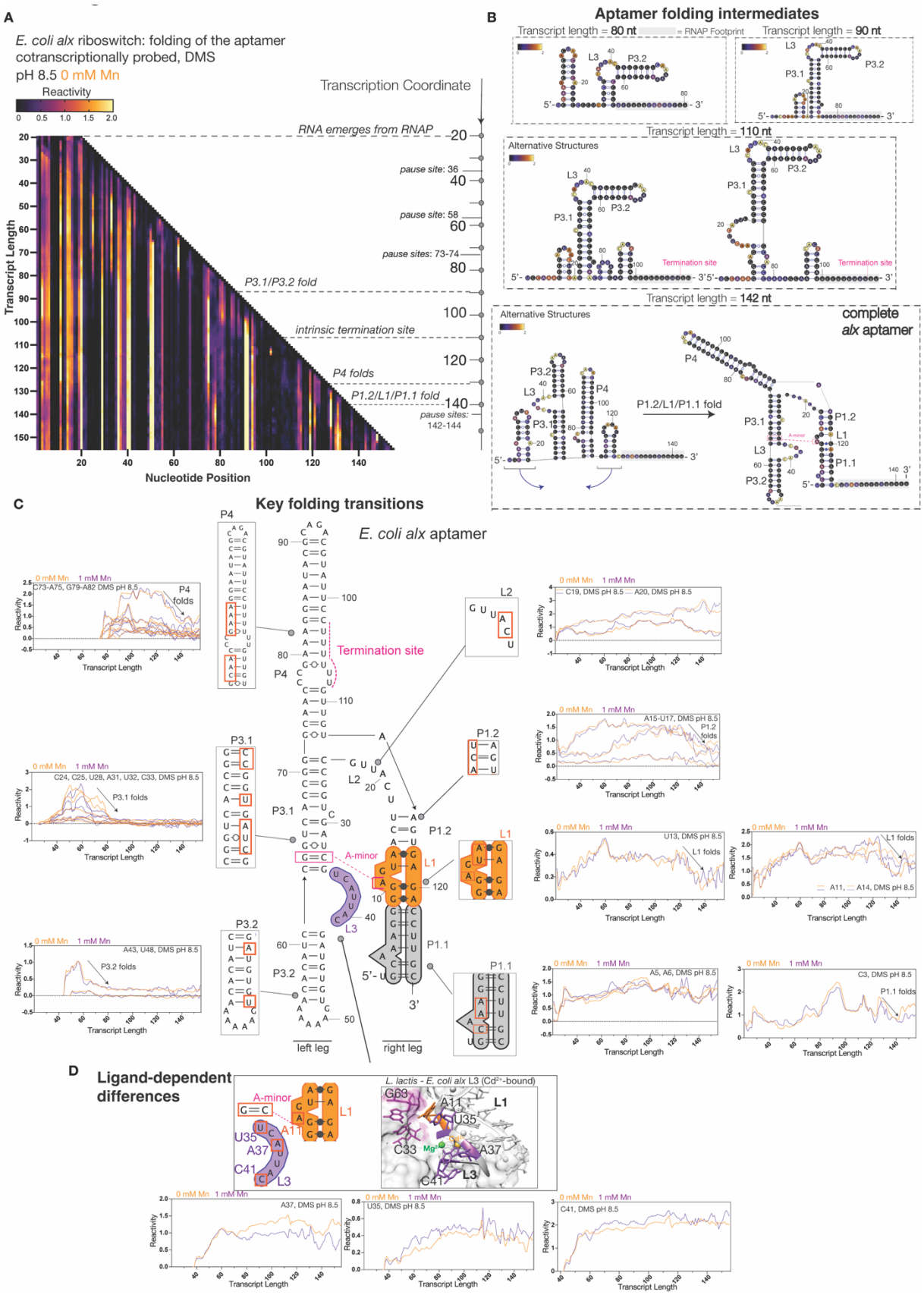
A
E. coli alx riboswitch: folding of the aptamer cotranscriptionally probed, DMS
pH 8.5 0 mM Mn
Reactivity
Transcription Coordinate
RNA emerges from RNAP
pause site: 36
pause site: 58
pause sites: 73-74
P3.1/P3.2 fold
intrinsic termination site
P4 folds
P1.2/L1/P1.1 fold
pause sites: 142-144
Transcript Length
Nucleotide Position
B
Aptamer folding intermediates
Transcript length = 80 nt
= RNAP Footprint
Transcript length = 90 nt
Transcript length = 110 nt
Alternative Structures
Termination site
Transcript length = 142 nt
complete alx aptamer
P1.2/L1/P1.1 fold
C
Key folding transitions
E. coli alx aptamer
P4 folds
Termination site
P3.1 folds
P3.2 folds
A-minor
left leg
right leg
L1 folds
P1.1 folds
Transcript Length
D
Ligand-dependent differences
L. lactis - E. coli alx L3 (Cd2+-bound)

1166

1167 **Figure 4. Co-transcriptional DMS probing of the *alx* riboswitch aptamer at alkaline**
1168 **pH. A.** TECprobe-VL DMS reactivity matrix for the *alx* aptamer at pH 8.5. Reactivities
1169 shown were normalized with a single, whole-dataset calculated normalization factor. Data
1170 are from seven independent replicates that were concatenated and analyzed together. **B.**
1171 Secondary structures of *alx* aptamer folding intermediates, which are colored by the DMS
1172 reactivity of the indicated transcript at pH 8.5. **C.** Transcript length-dependent reactivity
1173 changes showing folding transitions of the *alx* aptamer at pH 8.5 ± 1 mM Mn. DMS data
1174 for 0 mM Mn (orange) and 1 mM Mn (purple) conditions from Fig. 4A and SI Fig. 7,
1175 respectively. Secondary structure model of *alx* aptamer with labeled structural domains.
1176 L1 (orange), L3 (purple), P1.1 (gray), and intrinsic termination site (pink) are highlighted.
1177 Nt boxed in red correspond to adjacent nt reactivity plots. **D.** *L. lactis* Mn-sensing aptamer
1178 with *E. coli alx* L3 sequence (PDB ID: 6CC1). L3 nt (purple), cross-helix A-minor nt: A11
1179 (orange) and G63-C33 (magenta), Mg^{2+} (green sphere), and Cd^{2+} (yellow sphere) are
1180 highlighted. Plots show transcript length- and Mn-dependent reactivity changes in *alx*
1181 aptamer folding intermediates at pH 8.5 ± 1 mM Mn. DMS data for 0 mM (orange) and 1
1182 mM (purple) conditions from Fig. 4A and SI Fig. 7, respectively.
1183
1184

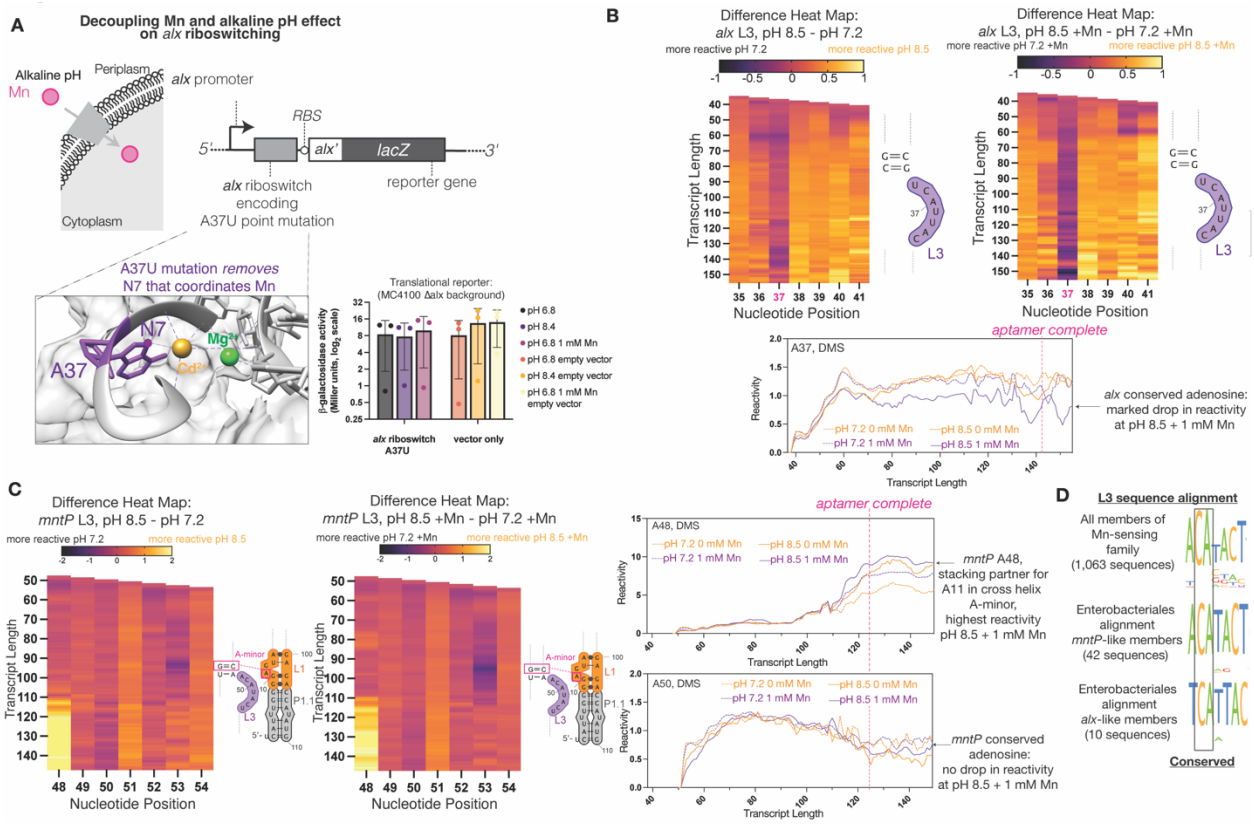

Figure 5. Decoupling the effects of alkaline pH and Mn on *alx* riboswitching *in vivo* and pH-dependent reactivity changes in the divergent *alx* and *mntP* L3 sequences. **A.** (Top panel) *E. coli* cell with increased cytosolic [Mn] resulting from an alkaline pH challenge (left) and construct design for *alx* translational reporter (right). (Bottom panel) *L. lactis* Mn-sensing aptamer with *E. coli alx* L3 sequence (PDB ID: 6CC1, left). Conserved A37 (purple), Mg^{2+} (green sphere), and Cd^{2+} (yellow sphere) are highlighted. (Bar graph) Loss of *alx* translational response to either Mn or pH upon mutation of the Mn-coordinating adenosine. **B-C**. Reactivity difference heatmaps and reactivity changes in aptamer intermediates for *alx* L3 nt (**B**) and *mntP* L3 nt (**C**) during aptamer folding at pH 7.2 vs. 8.5 ± 1 mM Mn. *alx* L3 and *mntP* L3 (purple), L1 (orange), L3 (purple), P1.1 (gray), and cross-helix A-minor (pink) are highlighted. DMS data for 0 mM Mn (orange) and 1 mM Mn (purple) conditions from Fig. 4A, SI Fig. 7, and SI Fig. 9B (**B**, *alx*) and Fig. 3A, SI Fig. 3, and SI Fig. 9A (**C**, *mntP*). Vertical dotted line marks completion of aptamer folding. **D.** L3 consensus sequences from *yybP-ykoY* family members in the Rfam database (top) and *mntP*-like (middle)/ *alx*-like (bottom) members in the *Enterobacteriales* order.

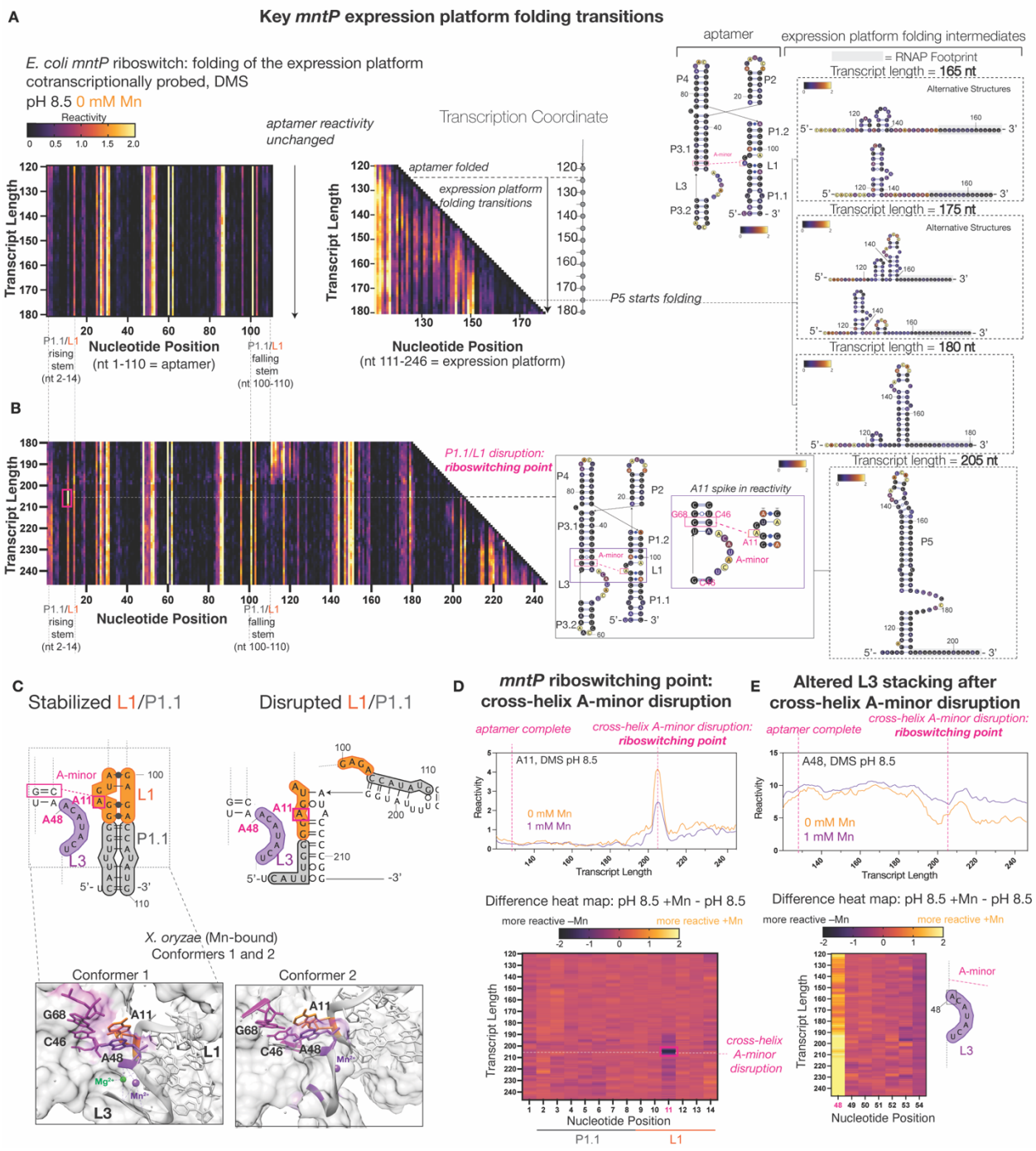
A
Key mntP expression platform folding transitions
E. coli mntP riboswitch: folding of the expression platform
cotranscriptionally probed, DMS
pH 8.5 0 mM Mn
Reactivity
aptamer reactivity unchanged
Transcription Coordinate
aptamer folded
expression platform folding transitions
P5 starts folding
Transcript Length
Nucleotide Position
(nt 1-110 = aptamer)
(nt 111-246 = expression platform)
P1.1/L1 rising stem (nt 2-14)
P1.1/L1 falling stem (nt 100-110)
aptamer
expression platform folding intermediates
= RNAP Footprint
Transcript length = 165 nt
Transcript length = 175 nt
Transcript length = 180 nt
Transcript length = 205 nt
Alternative Structures
B
P1.1/L1 disruption: riboswitching point
A11 spike in reactivity
A-minor
C
Stabilized L1/P1.1
Disrupted L1/P1.1
X. oryzae (Mn-bound) Conformers 1 and 2
Conformer 1
Conformer 2
D
mntP riboswitching point: cross-helix A-minor disruption
aptamer complete
cross-helix A-minor disruption: riboswitching point
A11, DMS pH 8.5
0 mM Mn
1 mM Mn
Reactivity
Transcript Length
Difference heat map: pH 8.5 +Mn - pH 8.5
more reactive –Mn
more reactive +Mn
cross-helix A-minor disruption
Nucleotide Position
P1.1
L1
E
Altered L3 stacking after cross-helix A-minor disruption
A48, DMS pH 8.5
A-minor
L3

1216 **Figure 6. Co-transcriptional DMS probing of the *mntP* riboswitch during expression**
1217 **platform folding. A-B**. (Left panel) TECprobe-VL DMS reactivity matrices of *mntP*
1218 riboswitch at pH 8.5. Reactivities shown were normalized with a single, whole-dataset
1219 calculated normalization factor. Data are from two independent replicates that were
1220 concatenated and analyzed together. (Right panel) Secondary structures of *mntP*
1221 expression platform folding intermediates colored by DMS reactivity of the indicated
1222 transcript at pH 8.5. **C.** (Top panel) Truncated secondary structure models of *mntP*
1223 riboswitch with a stabilized L1/P1.1 (Mn-bound) or disrupted L1/P1.1 (Mn-unbound).
1224 L1(orange), L3 (purple), P1.1 (gray), and cross-helix A-minor interaction (pink) are
1225 highlighted. (Bottom panel) *X. oryzae* aptamer metal-sensing core (PDB ID: 6N2V) with
1226 Mg^{2+} (green sphere) and Mn^{2+} (purple sphere) highlighted. Conformer 1 shows Mn^{2+} fully
1227 bound and Conformer 2 shows Mn^{2+} partially bound. A11 (orange) and A48 (purple) are
1228 highlighted. **D-E.** (Top panels) Transcript length- and Mn-dependent reactivity changes in
1229 A11 (**D**) and A48 (**E**) showing cross-helix A-minor disruption. (Bottom panels) Reactivity
1230 difference heatmaps for P1.1/L1 (**D**) and L3 (**E**) at pH 8.5 ± 1 mM Mn. DMS data for 0
1231 mM and 1 mM Mn conditions from Fig. 6A-B and SI Fig. 12A, respectively. Vertical or
1232 horizontal dotted lines mark indicated RNA folding transitions.
1233
1234

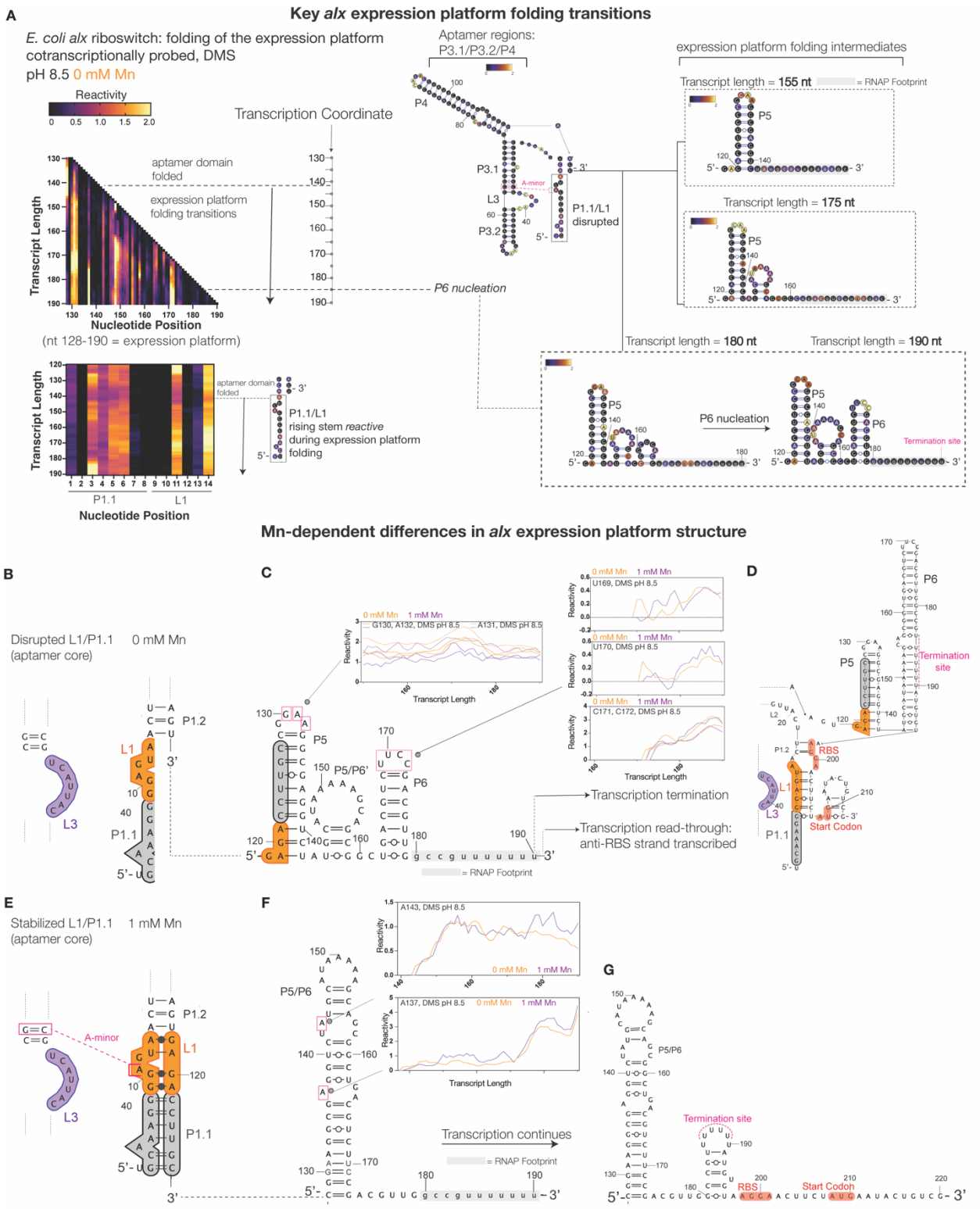
A
Key alx expression platform folding transitions
E. coli alx riboswitch: folding of the expression platform cotranscriptionally probed, DMS
pH 8.5 0 mM Mn
Reactivity
Transcription Coordinate
aptamer domain folded
expression platform folding transitions
Transcript Length
Nucleotide Position
(nt 128-190 = expression platform)
P6 nucleation
Aptamer regions: P3.1/P3.2/P4
P4
P3.1
L3
P3.2
A-minor
P1.1/L1 disrupted
expression platform folding intermediates
Transcript length = 155 nt
= RNAP Footprint
Transcript length = 175 nt
Transcript length = 180 nt
Transcript length = 190 nt
P5
P6
P6 nucleation
Termination site
P1.1/L1 rising stem reactive during expression platform folding
P1.1
L1
Mn-dependent differences in alx expression platform structure
B
Disrupted L1/P1.1 0 mM Mn
(aptamer core)
P1.2
P1.1
L3
C
0 mM Mn
1 mM Mn
G130, A132, DMS pH 8.5
A131, DMS pH 8.5
U169, DMS pH 8.5
U170, DMS pH 8.5
C171, C172, DMS pH 8.5
Reactivity
Transcript Length
P5
P5/P6'
P6
Transcription termination
Transcription read-through: anti-RBS strand transcribed
= RNAP Footprint
D
P6
P5
Termination site
RBS
Start Codon
L1
L3
P1.1
E
Stabilized L1/P1.1 1 mM Mn
(aptamer core)
A-minor
P1.2
L1
L3
P1.1
F
A143, DMS pH 8.5
A137, DMS pH 8.5
P5/P6
Transcription continues
= RNAP Footprint
G
P5/P6
Termination site
RBS
Start Codon

1239 **Figure 7. Co-transcriptional DMS probing of the *alx* riboswitch during expression**
1240 **platform folding. A.** (Left panel) TECprobe-VL DMS reactivity matrix of the *alx*
1241 expression platform (top) and L1/P1.1 rising stem (bottom) at pH 8.5. Reactivities shown
1242 were normalized with a single, whole-dataset calculated normalization factor. Data are
1243 from seven independent replicates that were concatenated and analyzed together. (Right
1244 panel) Secondary structures of *alx* folding intermediates colored by DMS reactivity of the
1245 indicated transcript at pH 8.5. **B.** Truncated secondary structure model of the *alx* aptamer
1246 with a disrupted L1/P1.1 (Mn-unbound). L1 (orange), L3 (purple), and P1.1 (gray) are
1247 highlighted. **C.** Secondary structure model of *alx* expression platform at transcript length
1248 190 nt –Mn. L1 falling stem (orange) and P1.1 falling stem (gray) paired in P5 are
1249 highlighted. Adjacent to nt boxed in pink are plots with their respective transcript-length
1250 and Mn-dependent reactivity changes. DMS data for 0 mM (orange) and 1 mM Mn
1251 (purple) conditions are from Fig. 7A and SI Fig. 15A, respectively. **D.** Secondary structure
1252 model of full-length, translationally inactive *alx* expression platform with same aptamer
1253 color scheme as in panels A-B. RBS/start codon (red) and P6 intrinsic terminator stem
1254 (pink) are highlighted. **E.** Truncated secondary structure model of the *alx* aptamer with a
1255 stabilized L1/P1.1 (Mn-bound) with same aptamer color scheme as in panel A. Cross-
1256 helix A-minor motif (pink) is highlighted. **F.** Secondary structure model of *alx* expression
1257 platform at transcript length 190 nt +Mn. Adjacent to nt boxed in pink are plots with their
1258 respective transcript-length and Mn-dependent reactivity changes. DMS data for 0 mM
1259 (orange) and 1 mM Mn (purple) conditions are from Fig. 7A and SI Fig. 15A, respectively.
1260 **G.** Secondary structure model of full-length, translationally active *alx* expression platform
1261 with same aptamer color scheme as in panel D. RBS/start codon (red) and intrinsic
1262 termination site in inactive conformer (pink) are highlighted.
1263
1264
1265

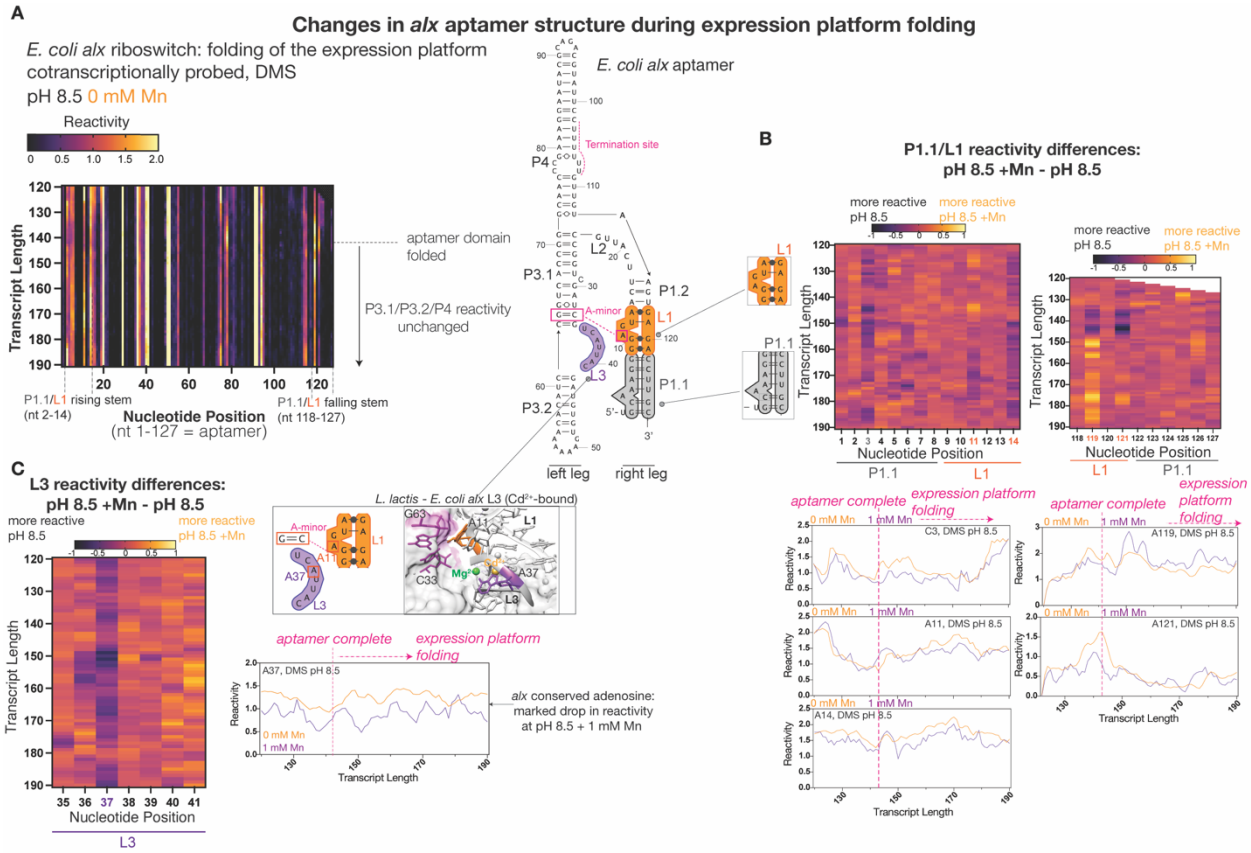

Figure 8. Changes in the *alx* aptamer during expression platform folding. A. (Left panel) TECprobe-VL DMS reactivity matrix of the *alx* riboswitch aptamer during expression platform folding at pH 8.5. Reactivities shown were normalized with a single, whole-dataset calculated normalization factor. Data are from seven independent replicates that were concatenated and analyzed together. (Right panel) Secondary structure model of *alx* aptamer with labeled structural domains. L1 (orange), L3 (purple), P1.1 (gray), and intrinsic termination site (pink) are highlighted. **B-C.** Reactivity difference heatmaps for L1/P1.1 (**B**) and L3 (**C**) at pH 8.5 ± 1 mM Mn. Adjacent to heatmaps are transcript length- and Mn-dependent reactivity changes in L1/P1.1 nt (**B**) and L3 nt (**C**). DMS data for 0 mM and 1 mM Mn conditions from Fig. 8A and SI Fig. 15A, respectively. Vertical or horizontal dotted lines/arrows mark indicated RNA folding transitions. *L. lactis* Mn-sensing aptamer with *E. coli alx* L3 sequence (PDB ID: 6CC1) shown in panel B with A37 (purple), cross-helix A-minor nt: A11 (orange) and G63-C33 (magenta), Mg^{2+} (green sphere), and Cd^{2+} (yellow sphere) highlighted.

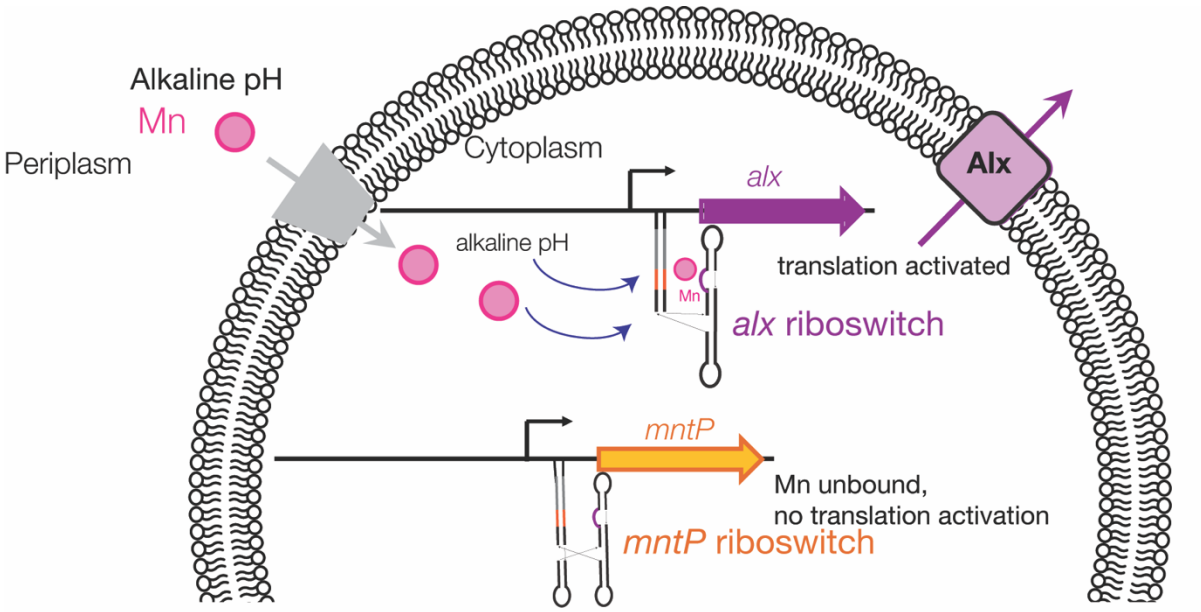

Figure 9. Model for *alx* and *mntP* riboregulation in *E. coli*. Cartoon model of *alx* and *mntP* riboregulation of their respective genes in *E. coli*. At alkaline pH, the cytosolic [Mn] increases, resulting in the *alx* riboswitch turning "on" expression of Alx to prevent toxic accumulation of Mn in the cytosol. The modest increase in cytosolic [Mn] brought about by alkaline pH is insufficient to shift the *mntP* riboswitch towards its translationally active conformation, leaving *mntP* expression "off".

Acknowledgements

We thank Dr. Eric Strobel and Dr. Courtney Szyjka for protocols and helpful discussions regarding TECprobe-VL experiments. We also thank members of our research group for their valuable feedback during the course of this study. This work was supported by the National Institutes of Health (NIGMS ESI grant R35GM142785), Burroughs Wellcome Fund CASI (grant no.: 1016945) to T.V.M., UCSD institutional support, and Yinan Wang Memorial Chancellor's Endowed Junior Faculty Fellowship to T.V.M. This material is based upon work supported by the National Science Foundation Graduate Research Fellowship Program under Grant No. DGE-2038238 to D.P. Any opinions, findings, and conclusions or recommendations expressed in this material are those of the author(s) and do not necessarily reflect the views of the National Science Foundation.

Author contributions

C.S. and T.V.M, conceptualization; C.S. and D.P., methodology; C.S. and D.P., investigation; C.S. and D.P., formal analysis; C.S. and D.P., visualization; C.S. and D.P., writing-initial draft; C.S., D.P., and T.V.M, writing-review and editing; T.V.M, supervision; T.V.M., funding acquisition.

Competing Interests

The authors declare no competing interests.